



Simultaneously enhancing strength and ductility of coarse grain Cu–Al alloy via a macro dual-cable structure

Kaixuan Zhou^{a,1}, Yonghao Zhao^{a,b,*,1}, Qingzhong Mao^a, Ruisheng Zhang^a, Shunqiang Li^a, Guosheng Sun^a, Hongzhen Dong^a, Lei Gu^a, Jizi Liu^{a,c,**}

^a Nano and Heterogeneous Materials Center, Nanjing University of Science and Technology, Nanjing, 210094, China

^b School of Materials Science and Engineering, Hohai University, Changzhou, 213200, China

^c Center of Analytical Facilities, Nanjing University of Science and Technology, Nanjing, 210094, China

ARTICLE INFO

Handling Editor: Dr Hao Wang

Keywords:

Strength and ductility
Dual-cable structure
Cu–Al alloy
Shear band
Strain hardening

ABSTRACT

The trade-off relationship of strength and ductility of metals leads to a strength increase accompanied by a ductility decrease. In the past two decades, despite significant efforts to increase strength while minimizing the ductility loss by tailoring microstructures, it has been rare to achieve simultaneous enhancement in strength and ductility, i.e., to disrupt the trade-off relationship. Here via rotary swaging and subsequent annealing, we prepared a macro dual-cable structured Cu–Al alloy rod with an inner micro-grain (MG) core (2.2 mm in diameter, 54% volume fraction) wrapped in an outer ultrafine-grain (UFG) shell (a thickness of 0.4 mm). Tensile tests revealed that the inner core has a yield strength of 472 MPa and a ductility of 29.1%, while the wrapping of the outer shell simultaneously enhances the yield strength to 552 MPa and ductility to 31.9%, respectively. The analysis of strain during the stretching process shows that the shell has a strong restraining effect on the core. Microstructure characterization indicates that the core blocks the propagation of the shear bands of shell and maximizes its density. At the same time, the restriction of the shell increases the lattice defect accumulation and work hardening ability as well as ductility of the core. Our research not only provides a method for preparing macro dual-cable structured materials with industrial scale and clean interface, but also explores a new strategy for simultaneously enhancing strength and ductility of metals, which designs macro millimeter-scale structures instead of adjusting microstructure from the micrometer scale.

1. Introduction

Strength and ductility, as the two basic mechanical properties of structural materials, are often inherently trade-off with each other [1,2]. As shown in Fig. 1, strength and ductility exhibit an inverse relationship (dashed black curve), that is, as the strength slowly increases, the ductility loses rapidly. This law also applies to nanostructured materials that have been widely studied in the past forty years [3]. Numerous studies have shown that nanostructured materials have high strength but low ductility which can cause uncontrollable catastrophic fracture failures and safety accidents during service.

To improve the poor ductility of nanostructured metals, many strategies including removing manufacturing artifacts [4,5], bi-/multi-modal grain size distributions [6], transformation-induced-plasticity (TRIP)

and twinning-induced-plasticity (TWIP) effects [7,8], nanotwinned grains [9], nanoscale precipitates/dispersions in nanostructured metallic materials [10], nano-gradient structure [11], lamellar structure [12], heterogeneous lamellar structure [13], harmonic structure [14], etc. have been proposed in the last twenty years. As summarized in Fig. 1, the optimized heterogeneous lamellar Cu/Cu–Zn and Cu with bi-modal grain size distributions can exhibit a linear strength-ductility relationship with a negative slope (dashed blue and green lines). Nano-gradient structure also can further improve the strength-ductility relationship (dashed purple line), i.e., with a rapid increase in strength, the loss of ductility is slow. Nevertheless, almost all data points for face centered cubic (FCC) metals are located in the left half of Fig. 1, which means that the above strategies can only improve, but not break the strength-ductility inverse relationship. However, we were surprised to

* Corresponding author. Nano and Heterogeneous Materials Center, Nanjing University of Science and Technology, Nanjing 210094, China.

** Corresponding author. Nano and Heterogeneous Materials Center, Nanjing University of Science and Technology, Nanjing 210094, China.

E-mail addresses: yhzhao@njust.edu.cn (Y. Zhao), jzliu@njust.edu.cn (J. Liu).

¹ These two authors contributed equally to this work.

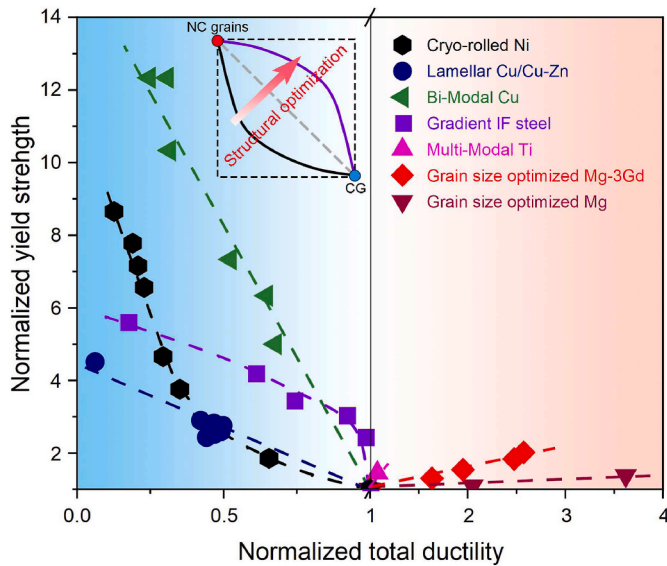


Fig. 1. Literature data summary and comparative analysis of normalized yield strength versus normalized (ratio to coarse grain (CG)) total ductility of FCC cryo-rolled Ni [15], lamellar Cu/Cu-Zn [16], bi-modal Cu [17], gradient IF steel [18], HCP Ti [6], Mg-3Gd alloys [19], and Mg [20].

find that some data points of hexagonal closely packed (HCP) Mg and Ti alloys, ran to the right half of Fig. 1, indicating increases in both strength and ductility and a subversion of the strength-ductility trade-off relationship, although their other data points also fell to the left half of Fig. 1. Further in-depth research revealed that, the strength increase, caused by the reduction of the grain size of Mg alloy and the local stress concentration of multi-modal Ti, activated the additional $\langle c+a \rangle$ etc. non-basal dislocation slip systems, thereby increasing the work hardening rate and ductility. The $\langle c+a \rangle$ etc. non-basal dislocation slip systems of coarse-grained Mg or Ti are difficult to activate due to their high critical resolved shear stress (CRSS) that is one order of magnitude larger than basal slip system. This enlightens us that if we want to increase strength and ductility simultaneously, we must initiate new extra slip systems to increase work hardening rate at the same time of strengthening. Now the question is can we achieve simultaneous increases in strength and ductility for FCC metals which only have 12 equivalent 111 slip systems? Different from the HCP metals with different CRSSes for $\langle a \rangle$, $\langle c \rangle$ and $\langle c+a \rangle$ slip systems, the 12 equivalent 111 slip systems in FCC metals has the same CRSS. Moreover, up to now, all strategies for improving strength-ductility trade-off relationship are achieved by adjusting the microstructure at the micrometer level, and can we improve the strength-ductility combination by designing macro millimeter-scale structures?

To answer the above two questions, in this work, we prepared a macro dual-cable structured (DCS) Cu-15at.% Al alloy rod with low stacking fault energy (SFE) of $\sim 6 \text{ mJ m}^{-2}$ [21] and with an inner micro-grain (MG) rod-shaped core (2.2 mm in diameter) wrapped in an outer ultrafine-grain (UFG) cylinder-shaped shell (1.8 mm in thickness) via rotary swaging (RS) and subsequent annealing. We found the DCS Cu-Al alloy has both higher strength and ductility than the individual MG core counterpart. Microstructure characterization indicates that the outer UFG shell increases the work hardening ability of the MG core, and the MG core blocks the propagation of the shear band (SB) of UFG shell. Our research verifies the possibility of simultaneously enhancing strength and ductility of FCC metals via designing macro millimeter-scale structures.

2. Materials and methods

2.1. Preparation process of DCS Cu-Al alloy

The as-received $\text{Ø}20 \times 200 \text{ mm}$ Cu-15 at. % Al rods were first homogenized at 1073 K for 2 h, the RS process was then performed at room temperature. The working principle was schematically represented in Fig. 2a. The forging hammers rotate at high speed around the Cu-Al rod driven by the main shafts, and simultaneously apply high-frequency small-strain forging to the rod, gradually refining and elongating the Cu-Al rod. Through multiple passes, a $\text{Ø}5.7 \times 2400 \text{ mm}$ rod was finally prepared (Fig. 2b), corresponding to an equivalent strain (ϵ) of 2.5, designated as sample DCS1. The ϵ was calculated by the formula of $\epsilon = \ln(A_0/A)$, where A_0 and A are the initial and final cross-sectional areas, respectively. Sample DCS1 was then annealed at 573 K for 1 h to obtain another type of DCS structure, designated as sample DCS2. In addition, due to the axial symmetry of the materials prepared by RS, observation planes (top view and side view) and directions (axial direction (AD) and radial direction (RD)) are defined, as shown in Fig. 2a.

2.2. Mechanical property tests

Vickers microhardness tests were performed using an HMV-G 21DT (Shimadzu, Japan) tester with a load of 1.96 N and a dwell time of 10 s in conventional samples. To obtain more accurate spatial resolution, a load of 0.49 N was selected for hardness testing on tensile specimens with different deformation. Ten indentations were tested to obtain reliable results.

Uniaxial tensile tests and digital image correlation (DIC) tests were performed using a w + b LFM20KN universal testing machine (Walter + Bai AG in Switzerland) and 3D optical measuring techniques (GOM Company in Germany) in quasi-static loading with a strain rate of $1 \times 10^{-3} \text{ s}^{-1}$ at room temperature. As shown in Fig. 4 in section 3.1, the swaged DCS1 sample has a hard inner nano-grained (NG) core with a diameter of 2.2 mm and a relatively soft outer UFG shell with a thickness of 1.8 mm, and the annealed DCS2 sample possesses a relatively soft inner MG rod-shaped core (2.2 mm in diameter) wrapped in an almost unchanged relatively hard outer UFG shell with a thickness of 1.8 mm. Then we performed tensile tests on the individual cores and individual shells as well as DCS1 and DCS2 samples with different combinations of core and shell. The gauge length of all tensile specimens was parallel to the swaging direction, and according to the ASTM E8/E8M, the ratio of gauge length to diameter is 5 to make the tensile curves of different specimens with different diameter comparable. Specifically, the tensile

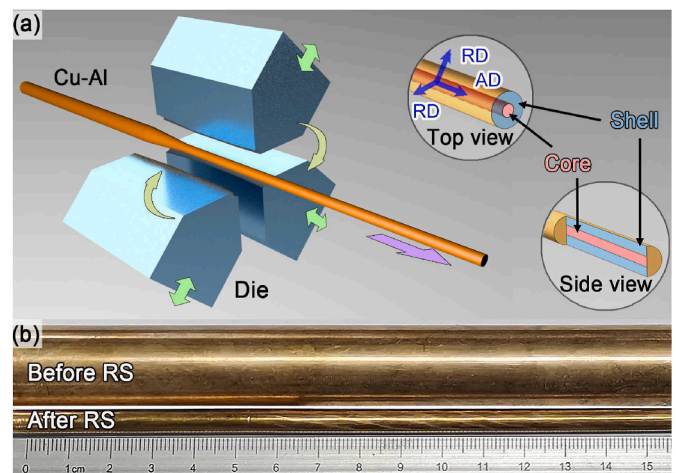


Fig. 2. (a) Schematic illustration of the RS technique and observation planes (top and side views) and directions (RD and AD) of the swaged rods. (b) Picture of the swaged Cu-Al samples with $\epsilon = 0$ and $\epsilon = 2.5$.

specimens for individual core or shell parts have gauge dimensions of $\text{Ø}1.2 \times 6$ mm, as shown in Fig. 3a. For samples DCS1 and DCS2, the gauge dimensions were selected as $\text{Ø}4 \times 20$ mm and $\text{Ø}3 \times 15$ mm, corresponding to 30% and 54% volume fraction of the inner NG/MG cores (with a diameter of approximately 2.2 mm), respectively, the sampling position of the stretching sample gauge section was shown in Fig. 3b. The tensile strain was measured by using a standard non-contacting video extensometer.

Due to the interface being wrapped inside the sample, in order to observe the behavior of the interface by DIC and quasi-in-situ electron backscatter diffraction (EBSD) during the deformation process, a $0.4 \times 4 \times 8$ mm plate-shaped tensile specimen was taken from the center of the circular rod, and the volume fraction of the inner core part in the total gauge is about 54%, the sampling position of the stretching sample gauge section was shown in Fig. 3c. The samples used in DIC were sprayed with white paint evenly first, and then sprayed with uniform black speckles through a 0.25 mm caliber spray gun. The size of a single speckle is about 25–75 μm , and an optical image covering 2048×1088 pixel² effective area with a spatial resolution of 5 μm /pixel was taken. The DIC data was then processed with ARAMIS software (GOM GmbH). Three tensile specimens were tested to obtain reliable results.

2.3. Thermal analysis

Thermal analysis was performed in a PerkinElmer (DSC8000) differential scanning calorimeter (DSC). The weight of each sample is about 30 mg. The polished samples were sealed in Al pans and heated in a flowing N₂ atmosphere at a constant heating rate of 20 K/min; an additional empty Al pan was used as a reference. Three samples were tested in order to ensure reproducibility of results.

2.4. Microstructural characterizations

The X-ray diffraction (XRD) scanning on the samples was carried out by Bruker D8 Discover with Co K α radiation. The scanning area is the circular area with a diameter of 1 mm, and the scanning Bragg angle range is 30–125°.

EBSD analysis was performed on a Zeiss Auriga focused ion beam/scanning electron microscope equipped with a fully automatic Oxford Instruments Aztec 2.0 EBSD system. Samples used for EBSD were first sandpaper polished, then electropolished on a Buehler ElectroMet@4 with 25% H₃PO₄ + 25% absolute alcohol + 50% deionized water electrolyte, a voltage of 8 V and polishing time of 30–60 s. Software Channel 5 was used to process the EBSD data. Olympus BX41 M (Japan) was used for taking optical microscope photos, the samples were subjected to 2–10 s of corrosion with 5 g FeCl₃ + 15 ml HCl + 80 ml deionized water after electro polishing.

The transmission electron microscope (TEM) observations were carried out on a FEI Tecnai 20 at a voltage of 200 kV, and high-resolution transmission electron microscopy (HRTEM) observations were carried out on a FEI Titan G2 at 300 kV with aberration corrected. Samples used for TEM first underwent machining and sanding to obtain 50 μm thick discs, then twin-jet polished in an electrolyte of 25% H₃PO₄ + 25% absolute alcohol + 50% deionized water at about 265 K. The residual surface phosphate was then removed with ion milling (Gatan 695).

A Thermo Fisher Scientific Spectra 300 microscope with double correctors was used for characterize the microstructure of NGs. Scanning precession electron diffraction (SPED) was performed using NanoMEGAS (Belgium) DigiSTAR P2010 precession and scan generator, the scan step is 5 nm. SPED data was then processed through NanoMEGAS ASTAR software. The sample preparation method for SPED is the same as that for TEM.

3. Results

3.1. Mechanical properties of DCS Cu–Al alloys

Fig. 4a and b shows the top-view microhardness distributions of DCS1 and DCS2, respectively. One can see that the swaged DCS1 sample has a hard inner core with a maximum microhardness of 320 HV and a diameter of 2.2 mm, and a relatively soft outer shell with a microhardness of 250 HV and a thickness of 1.8 mm. However, annealing caused a reverse dual-cable structures of DCS2, that is, a relatively soft inner core with a microhardness of 200 HV and a diameter of 2.2 mm, and an almost unchanged relatively hard shell with a microhardness of 250 HV and a thickness of 1.8 mm. Moreover, the microhardness changes sharply at the core-shell interfaces of both DCS1 and DCS2, and both core and shell have macroscopic sizes of millimeters, this phenomenon is also reflected in optical microscope photos in Fig. 4a and b, this is why we call “dual-cable structure” but gradient structure because the former seems to be able to more accurately describe the structural characteristics of our materials. It should be noted that our DCS is also different from heterogeneous lamellar structure from macroscopic geometric characteristics, the former is macro millimeter-scale rod-shaped core wrapped in the macro millimeter-scale cylinder-shaped shell, while the latter is the alternating arrangement of soft and hard layers with micrometer scale.

Fig. 4c shows tensile curves of individual inner core and outer shell with homogeneous structure (HGS) as well as DCS Cu–Al alloy rods with 30% and 54% volume fractions of inner core, respectively. The swaged inner core in DCS1 has the highest yield strength of 1016 MPa and ultimate tensile strength (UTS) of 1034 MPa, lowest total ductility of 4.8% and nearly null strain hardening capability (dashed green curve). The

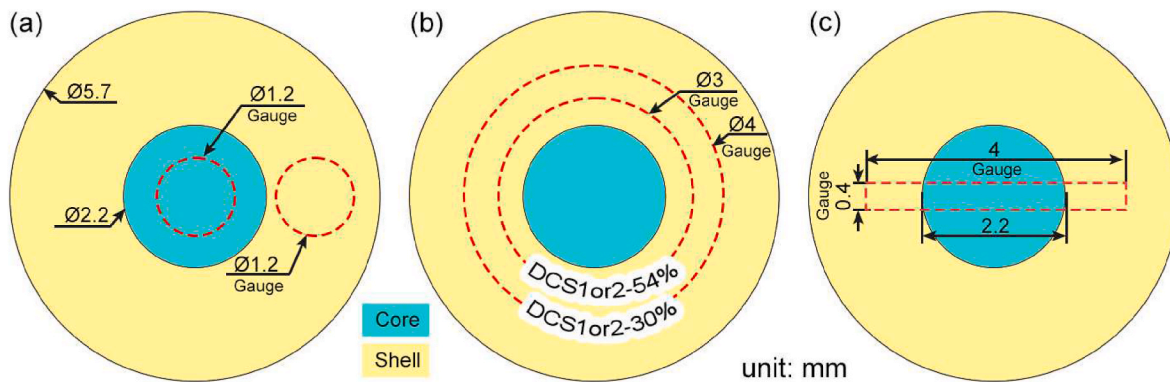


Fig. 3. The gauge sampling position and size for tensile testing on the top view. (a) Separate core and shell rod-shaped tensile samples with a gauge of 1.2 mm diameter. (b) DCS1 and DCS2 rod-shaped tensile samples with 54% and 30% core corresponding to gauge diameters of 3 mm and 4 mm, respectively. (c) Plate-shaped tensile samples with a $0.4 \times 4 \times 8$ mm gauge dimension for DIC and quasi-in-situ EBSD during the deformation process.

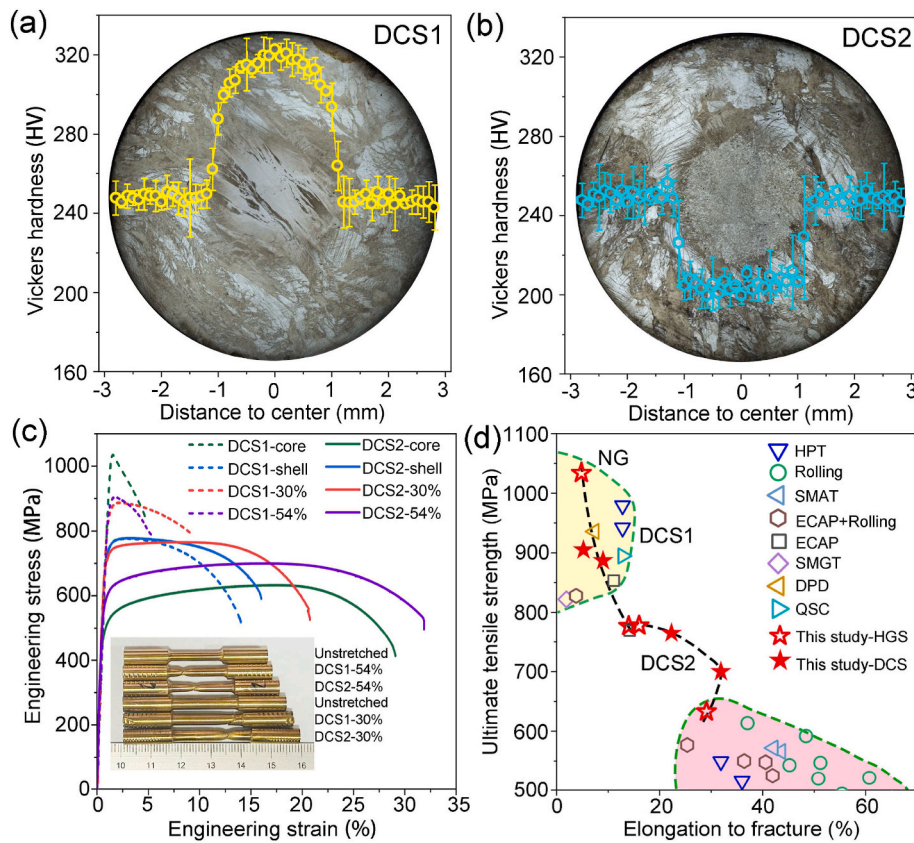


Fig. 4. Mechanical properties of sample DCS1 and DCS2. (a,b) Microhardness distributions of DCS1 and DCS2, respectively, the backgrounds are optical microscope photos of the top view of DCS1 and DCS2, respectively. (c) Tensile curves of swaged and annealed individual cores and shells in DCS1 and DCS2 as well as DCS Cu–Al alloy rods with 30% and 54% volume fractions of inner core, respectively. Inset is the unstretched and stretched tensile specimens. (d) Literature data summary and comparative analysis of UTS versus elongation to fracture of Cu–Al alloys obtained by different deformation methods [21–32]. SMAT, SMGT, ECAP, HPT, DPD, QSC and HGS are surface mechanical attrition treatment, surface mechanical grinding treatment, equal channel angular pressing, high pressure torsion, dynamic plastic deformation, quasi static compression and homogeneous structure, respectively.

values of yield strength, UTS, uniform elongation and elongation to fracture of the samples in this study were listed in Table 1. The swaged outer shell has much lower yield strength of 707 MPa and UTS of 777 MPa, higher total ductility of 14.0% (dashed blue curve). The annealed inner core in DCS2 has the lowest yield strength of 472 MPa and UTS of 633 MPa, higher uniform elongation of 16.9% and total ductility of 29.1%, respectively, as well as evident strain hardening capability (solid green curve). This is caused by the completely recrystallized MGs, as revealed in section 3.2. The annealed outer shell in DCS2 has nearly unchanged yield strength and UTS (solid blue curve) compared with that in DCS1, but slightly larger total ductility of 16% due to slightly lower dislocation density by annealing (revealed in section 3.2).

For the four swaged and annealed DCS tensile specimens containing both the inner core and the outer shell, we name them as DCS1-30%,

Table 1

Tensile properties of DCS1 and DCS2. $\sigma_{0.2}$, σ_{UTS} , ϵ_u and ϵ_f are yield strength, ultimate tensile strength, uniform elongation and elongation to fracture, respectively.

Samples		$\sigma_{0.2}$ (MPa)	σ_{UTS} (MPa)	ϵ_u (%)	ϵ_f (%)
DCS1	Core	1016	1034	1.5	4.8
	Shell	707	777	3.1	14.0
	30%Core	800	887	2.2	9.0
	54%Core	864	905	1.8	5.2
DCS2	Core	472	633	16.9	29.1
	Shell	691	778	3.6	16.0
	30%Core	683	765	8.6	22.3
	54%Core	552	700	16.5	31.9

DCS1-54%, DCS2-30%, and DCS2-54% based on the volume fraction proportion of the inner core in the gauge part. In DCS1, both samples have modest yield strength (800 and 864 MPa for DCS1-30% and DCS1-54%, respectively), UTS (887 and 905 MPa for DCS1-30% and DCS1-54%, respectively) and uniform elongation (2.2 and 1.8% for DCS1-30% and DCS1-54%, respectively) as well as total ductility (9.0 and 5.2% for DCS1-30% and DCS1-54%, respectively) compared with the tensile curves of the swaged individual core and shell. Fig. 5 illustrates the quantitative variation relationship between yield strength, UTS, uniform elongation and total ductility versus volume fraction of inner core. Therefore, one can conclude that the strength and ductility of the swaged four samples of DCS1-core, DCS1-54%, DCS1-30% and DCS1-shell basically follow the linear rule-of-mixtures [33] and strength-ductility trade-off relationship.

In DCS2, the DCS2-30% sample (solid red curve) has lower yield strength of 683 MPa and UTS of 765 MPa, and higher uniform elongation of 8.6% and total ductility of 22.3% compared with DCS2-shell, basically also complying with rule-of-mixtures and strength-ductility trade-off relationship when further comparing with the tensile curve of DCS2-core (Fig. 5). However, different from the varying trends of uniform elongation and ductility of DCS1-30%, DCS1-54% and DCS2-30%, the DCS2-54% sample (solid purple curve) has enhanced, but not reduced, total ductility of 31.9% and yield strength of 552 MPa as well as UTS of 700 MPa compared with the tensile curve of DCS2-core (solid green curve), that is, breaking the strength-ductility trade-off relationship and simultaneously increasing strength and ductility (Fig. 5c and d).

Fig. 4d represents the literature data summary and comparative

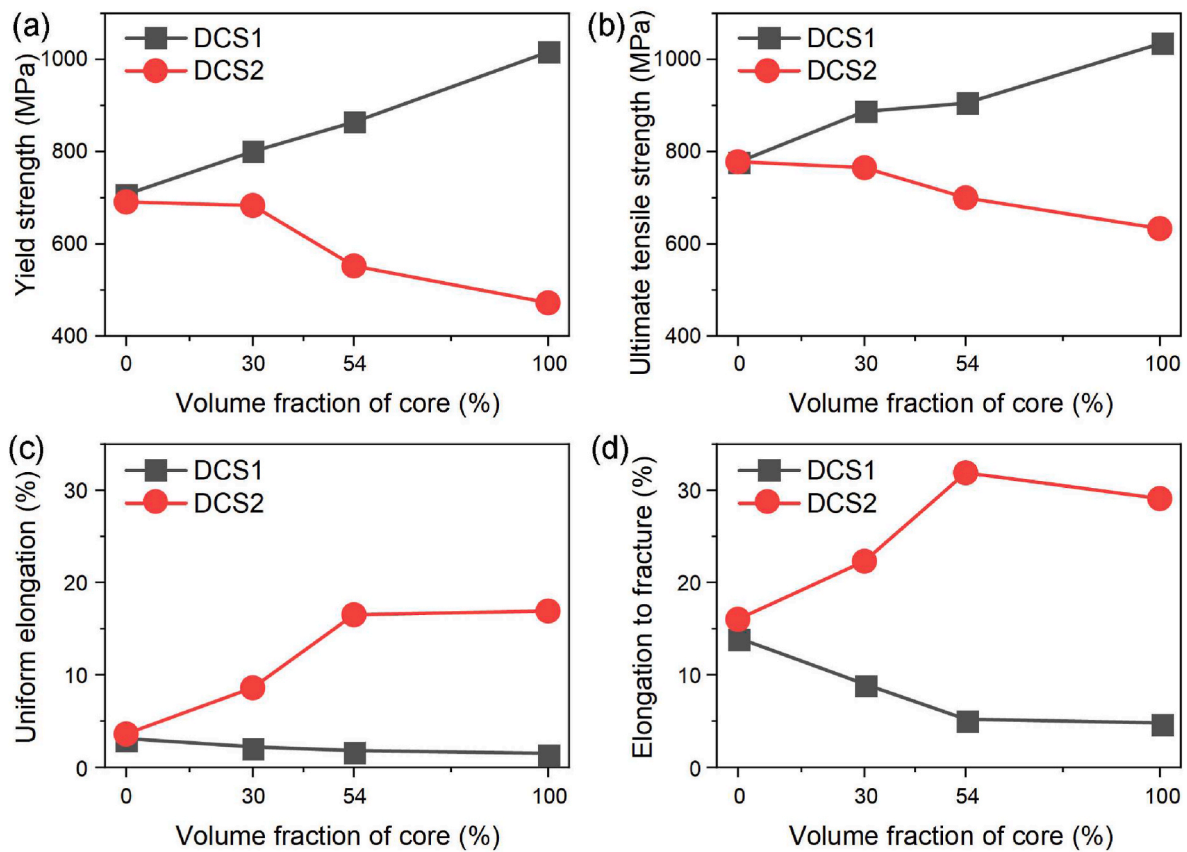


Fig. 5. Quantitative relationship between yield strength (a), UTS (b), uniform elongation (c) and ductility (d) versus volume fraction of inner core of swaged DCS1 and annealed DCS2 Cu–Al alloys. The strength and ductility of the swaged samples of DCS1-core, DCS1-54%, DCS1-30% and DCS1-shell as well as DCS2-core, DCS2-30% and DCS2-shell basically follow the linear rule-of-mixtures. Different from the varying trends of DCS1-30%, DCS1-54% and DCS2-30%, the DCS2-54% sample has enhanced, but not reduced, total ductility and yield strength as well as UTS compared with those of DCS2-core (100%).

analysis of UTS versus elongation to fracture of Cu–Al alloys obtained by different deformation methods and subsequent annealing [21–32]. Through comparison with literature, it was found that DCS1 follows the banana curve pattern of performance, while DCS2 exhibit reverse banana curve, the performance extends towards high strength and high elongation, and supplemented the performance gaps between the deformed NGs and the annealed MGs.

3.2. Microstructures of DCS Cu–Al alloys

Fig. 6 shows the microstructures of the swaged sample DCS1, after RS deformation, the average grain size at the inner core is about 45 nm from top view, as shown in Fig. 6a–d. From side view, the grains are slightly elongated along the rod axis (Fig. 6b), and the content of deformation twin boundaries (TBs) (take allowable error of $\pm 2^\circ$), high-angle grain boundaries (HAGBs) and low angle grain boundaries (LAGBs) are 30%, 25% and 45%, respectively (Fig. 6c). The outer shell of the rod contains dominant LAGBs (80%) and a certain number of SBs (Fig. 6e–h), the average size of sub-grains composed of LAGBs is about 0.3 μm (Fig. 6h). Side-view bright-field TEM images show that some elongated NGs in the inner core further contain a large number of nano-twins (Fig. 6i), and the SBs in the outer shell are composed of both UFGs and nano-twins (Fig. 6j).

Sample DCS2 is formed by annealing sample DCS1 at 573 K for 1 h, both top- and side-view EBSD revealed the inner core of the DCS2 has been fully recrystallized, and the average grain size is about 2.6 μm , as shown in Fig. 7a–d. There are a lot of annealing TBs (74%) in the recrystallized grains. HAGBs and LAGBs are relatively few, only covering 11% and 15%, respectively (Fig. 7c). For the shell, despite

undergoing the same annealing, the microstructures of the outer shell of DCS2 are similar to those of DCS1, which contain a large amount of LAGBs (80%) and SBs, the average sub-grain size is about 0.4 μm (Fig. 7e–h), Fig. 7i and j once again prove that the inner core recrystallized grains of DCS2 contain a large number of annealing twins, while the outer shell has similar microstructures with the sample DCS1. In addition, the HRTEM image of annealing TB in the inset of Fig. 7i indicates the coherent relationship. The geometric necessary dislocation density (ρ_{GND}) of two samples was quantified by EBSD and SPED data (Fig. 8), as listed in Table 2. The DCS1-core has the highest ρ_{GND} of $2.1 \times 10^{16} \text{ m}^{-2}$, and the annealed DCS2-core has the lowest ρ_{GND} of $4.2 \times 10^{14} \text{ m}^{-2}$. Both the outer shells of DCS1 and DCS2 have modest ρ_{GND} values among which the deformed shell has a larger ρ_{GND} of $2.0 \times 10^{15} \text{ m}^{-2}$ than the annealed shell ($1.8 \times 10^{15} \text{ m}^{-2}$).

3.3. Deformation process of DCS Cu–Al alloys

3.3.1. Coordinated deformation of core and shell by DIC

In order to explore the deformation process of DCS materials, we carried out the DIC experiment for plate-shaped samples DCS2-54% and DCS1-54% to reveal their strain distributions during the tensile process, as shown in Fig. 9. For the convenience of the DIC experiment, the gauge size of the plate-shaped tensile specimen used for DIC is selected as $4 \times 0.4 \times 8 \text{ mm}$, and the volume ratio of the core to the shell is the same as DCS1-54% and DCS2-54%. Due to the differences in geometric shapes of tensile specimens between plate and round rod, the elongation to fracture of the plate specimens is slightly reduced compared to the rod specimens (Fig. 9e), however, the strength and uniform elongation are much less affected, suggesting the geometric shapes of tensile specimens

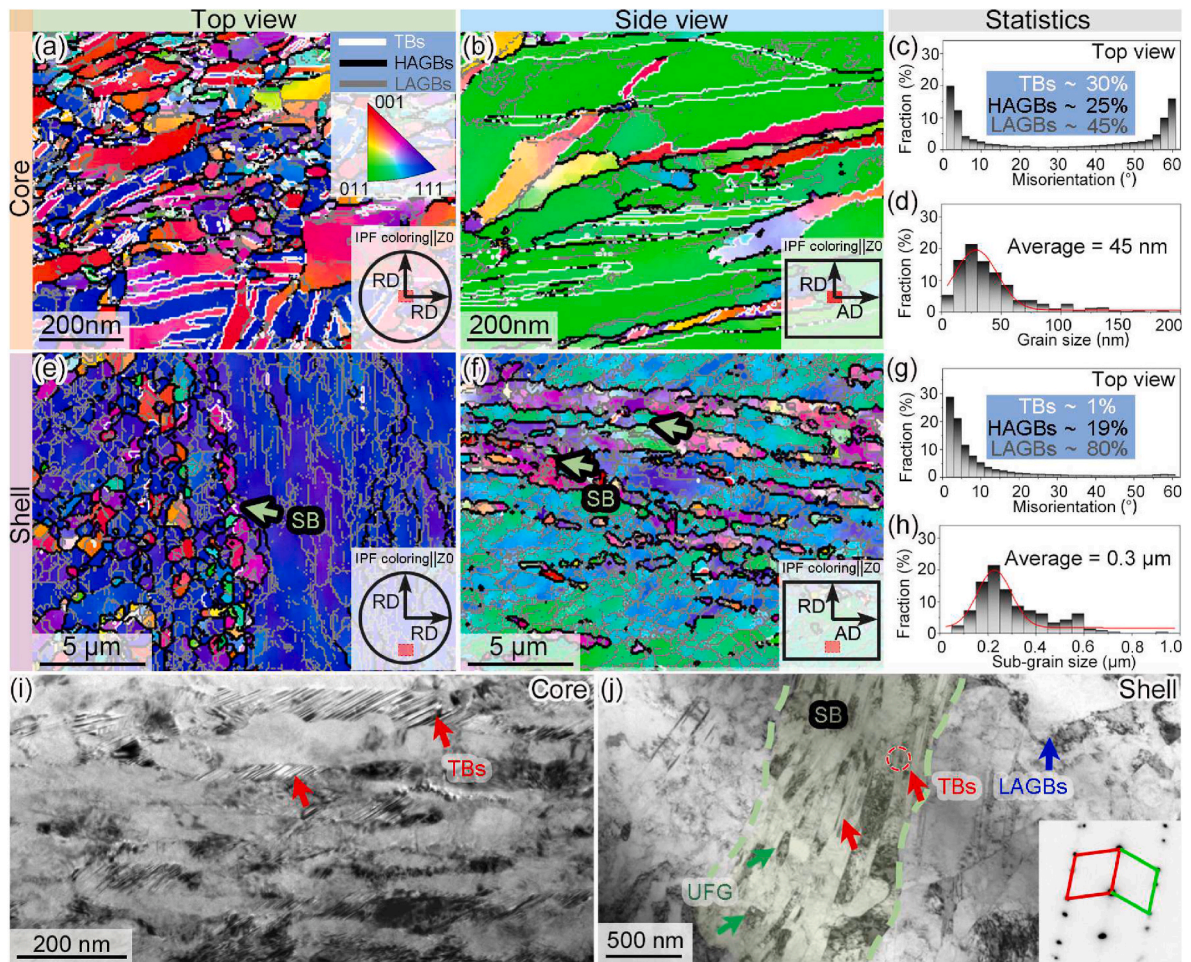


Fig. 6. Microstructures of sample DCS1. Top view (a,e) and side view (b,f) IPF + GB maps of the inner core (a,b) and outer shell (e,f). The inset in the bottom right corner shows the relationship between the three-dimensional coordinates of the detected plane and the sample, with the red area indicating the scanned area. The inset in the upper right corner of (a) is the legend of the line and area colors in the (a,b,e, and f). White, black, and gray lines representing $\Sigma 3$ TBs (the allowable error range is $\pm 2^\circ$), HAGBs ($>15^\circ$), and LAGBs (2° – 15°). GB misorientation distributions (c,g) and grain size distributions (d,h) of the inner core (c,d) and outer shell (g,h). (i,j) Side-view bright-field TEM images of the inner core and outer shell, the inset shows the SAED pattern from the circled area in (j). The red, green and blue arrows in (i) and (j) point to TBs, UFG grains, and LAGBs, respectively. The area between two dashed green lines in (j) is SB region. (For interpretation of the references to color in this figure legend, the reader is referred to the Web version of this article.)

has a greater impact on the post-necking elongation, local deformation after necking may accelerate in plate shaped specimens [34]. Therefore, analyzing the uniform deformation of the DCS samples by approximately using the plate tensile specimen is reasonable.

Fig. 9a and b shows the two-dimensional DIC distribution of DCS1 and DCS2 plate specimens, respectively, and Fig. 9c shows a schematic representation of optical measuring DIC techniques to measure the local strain field. Under the action of normal strain, the lattice is elongated in the tensile direction ($\varepsilon_{xx} = (L-L_0)/L_0$) and contracted in the cross-sectional direction ($\varepsilon_{yy} = (B-B_0)/B_0$). Under the action of shear strain, the lattice loses its orthogonal relationship, and the shear strain directions corresponding to positive and negative shear strains are different.

The one-dimensional average strain distribution curve along the gauge cross-section in the deformation region were shown in Fig. 9d. For the DCS1 sample, when the deformation is 0.7%, the distribution of ε_{yy} and ε_{xy} is relatively uniform. When the deformation reaches 1.2%, with the generation of macro-SBs passing through the specimen, there are about -3% for ε_{yy} at the intersection of the macro-SBs, ε_{xy} with opposite directions appears on both sides of the point. This phenomenon is more obvious at 2.4%. At the same time, a small amount of positive shear strain ε_{xy} is generated at the soft/hard interfaces near the macro-SBs, indicating a weak deformation coordination between soft shell and

hard core (Fig. 9a). The final fracture section is perpendicular to the tensile direction, and one of the shell sheets (lower part) still connected together, even if the core is already disconnected.

For the DCS2 sample, slightly normal strain ε_{yy} difference between the core and shell can be observed at 5% deformation (Fig. 9b–d), this phenomenon is more obvious in 15% and after necking, specifically, the absolute value of ε_{yy} of the core is higher than that of the shell, and the value is highest near the center (with a horizontal coordinate value of 0 mm), this indicates that the core is more inclined to be compressed in the y direction during deformation compared to the shell (Fig. 9d). For ε_{xy} , significant shear strains were generated on both sides of the core at the interface in 5%, and as the strain increases, the shear strain also increases and extends towards the interior of the core (Fig. 9d). For the necking stage (22%), two macro-SBs passed through the sample, and intersected at the core-shell interface. Like DCS1, the intersection of macro-SBs breaks first due to the largest strains at the intersection.

Fig. 9f is optical metallographic photo of the DCS2 tensile specimen surface when the tensile deformation strain is 15%. The inner core presents a dark color and high roughness, while the outer shells are bright and low roughness. Fig. 9g shows the enlarged area in the black dotted frame of Fig. 9f. The slip in the core results in cellular structure with a size similar to the grain size, while the outer shell has two types of high-density micro-SBs intersected with an angle of about 46° due to

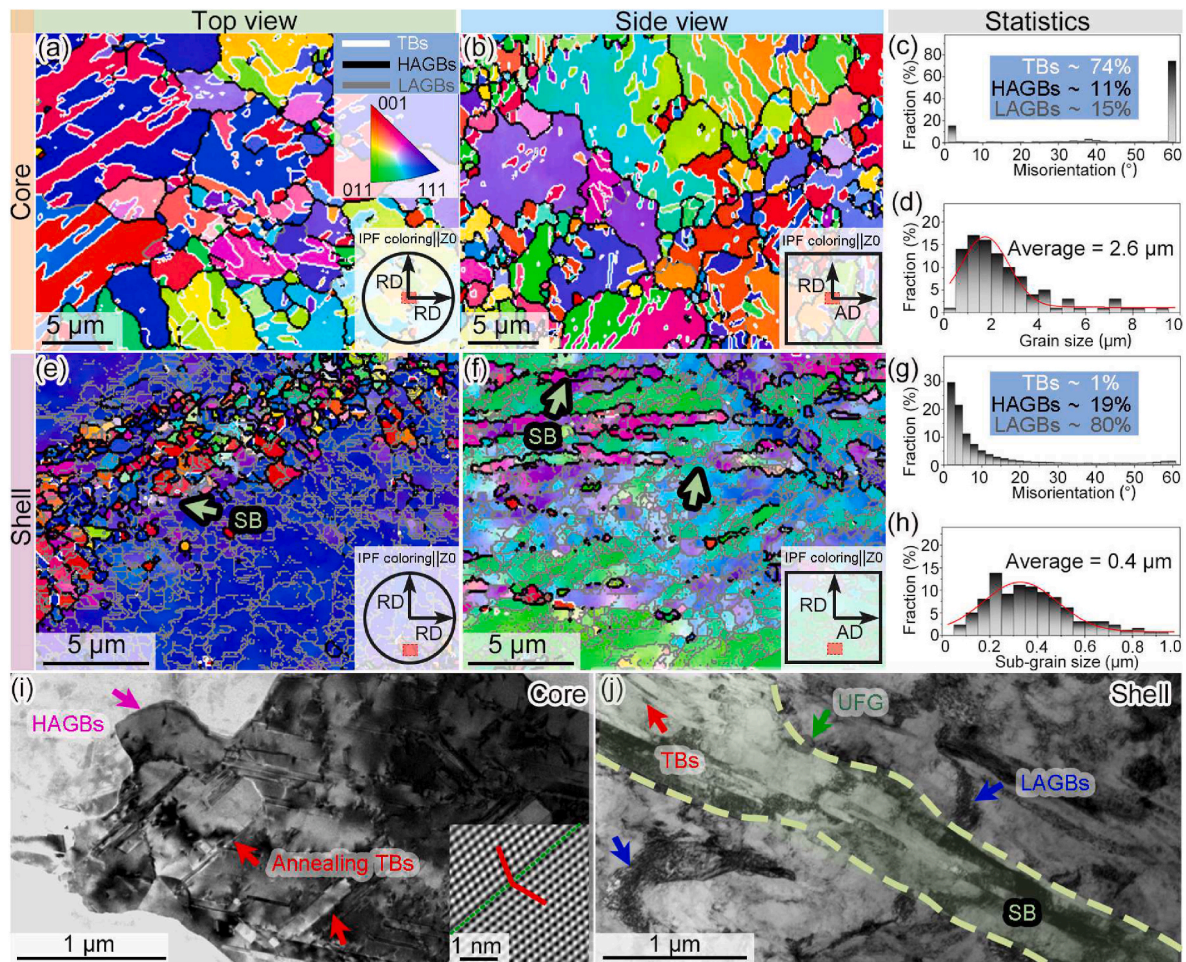


Fig. 7. Microstructures of sample DCS2. Top view (a,e) and side view (b,f) IPF + GB maps of the inner core (a,b) and outer shell (e,f), the meaning of the insets is the same as in Fig. 6. GB misorientation distributions (c,g) and grain size distributions (d,h) of the inner core (c,d) and outer shell (g,h). (i,j) Bright-field TEM images of the inner core (i) and outer shell (j). The inset in (i) is HRTEM image of annealing TBs. The red, green, pink and blue arrows point to TBs, UFGs, HAGBs and LAGBs, respectively. The area between two dashed green lines in (j) is SB region. (For interpretation of the references to color in this figure legend, the reader is referred to the Web version of this article.)

preferred orientation (Fig. 9f and g). Obviously, the micro-SBs do not pass through the interface until 15% tensile strain. During this process, the soft and hard zones can undergo collaborative deformation, improving the elongation. In addition, even during the necking stage, the ε_{yy} and ε_{xy} differences between core and shell still increases, indicating that the interaction between both is still enhanced, which may be an important reason why DCS2-54% has a higher total ductility compared to DCS2-core, despite having similar uniform elongation (Fig. 4c).

3.3.2. Micro-shear bands of the UFG shell by EBSD

It can be seen from the tensile curves that the uniform elongation of the shell is only 3.6%, while the sample DCS2-54% with a shell and core structure has a uniform elongation of about 16.5%. In order to explore how the shell uniformly deforms with the help of the core, quasi-in situ EBSD was used. As shown in Fig. 10, the core-shell interface of DCS2-54% is not a horizontal sharp line, but rather a convoluted interface due to the micro recrystallized grains neighboring with the non-recrystallized UFGs. After 5% tensile strain, there are more obvious micro-SBs in the hard shell (Fig. 10a2), and the Kernel average misorientation (KAM) in the MGs at the interface has significantly increased (Fig. 10c2), which corresponds to the increase of ρ_{GND} . When the strain is 13%, the number of micro-SBs in the hard-shell region is greatly increased (Fig. 10a3), the micro-SBs propagate and the core-shell interface moves about 10 μm towards the soft-core zone. However, the

local strain in the hard zone without micro-SBs (Fig. 10c3) is slightly lower than that in the 5% strain, indicating that the formation and propagation of micro-SBs produced strain release in the hard zone. The KAM in the soft core is greatly increased at 13% (Fig. 10c3), almost catching up with the hard-shell zone.

3.3.3. Strain hardening of the MG core by XRD and TEM

According to the Figs. 4c and 11a, it can be seen that DCS2-core and DCS2-54% have similar uniform elongation and work hardening rate (θ), although the shell has extremely low strain hardening ability and almost contributes null to the strain hardening of DCS2-54%. This means the core in the DCS2-54% sample must have higher strain hardening rate than the individual core, which therefore can make up for the strain hardening loss of the UFG shell. Moreover, from Fig. 11a, the work hardening rate of the plate-shaped tensile sample of DCS-54% is slightly lower than the rod-shape one, because the UFG shell only wraps the MG core from side part for the plate sample, while the hard shell wraps the MG rod core from 360° without dead corners for the rod-shaped sample. For ease of expression, the rod and plate tensile specimens of DCS2-54% in this paper are named as specimens A and B, respectively, while the rod tensile specimen of DCS2-core was named as specimen C, the schematic diagrams of sample location and size were also shown in the insets in Fig. 11a.

In order to investigate the source of high work hardening ability of sample DCS2-54%, hardness tests on tensile specimens under different

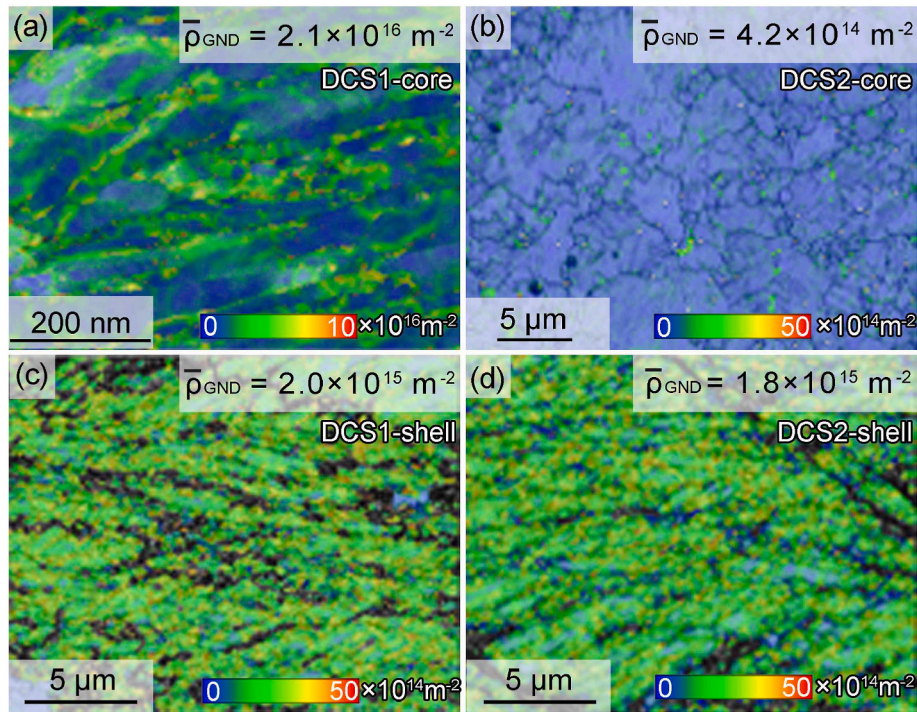


Fig. 8. Geometrically necessary dislocation density distribution of DCS1-core (a), DCS2-core (b), DCS1-shell (c), and DCS2-shell (d). The upper right corner is the average value.

Table 2

The volume fractions of TBs, HAGBs and LAGBs, average grain size, average geometrically necessary dislocation ρ_{GND} at different positions of two types of DCS Cu–Al alloys.

Sample	Position	TBs (%)	HAGBs (%)	LAGBs (%)	Grain size (nm)	ρ_{GND} (m^{-2})
DCS1	Core	25	30	45	45	2.1×10^{16}
	Shell	1	19	80	300	2.0×10^{15}
DCS2	Core	74	11	15	2600	4.2×10^{14}
	Shell	1	19	80	400	1.8×10^{15}

tensile strains were conducted. The hardness distributions of sample B with four different strains (0%, 5%, 10%, and 15%) were shown in Fig. 11b, it was found that with the increase of deformation, the hardness of the shell hardly changed, while the hardness of the core increased significantly, for 0%, 5%, 10%, and 15% deformation strain, the average hardness of the core was 195 HV, 210 HV, 216 HV, and 223 HV, respectively. This phenomenon coincides with the tensile curve in Fig. 4c, i.e., the shell has a very small strain hardening capacity compared to the core. Subsequently, by comparing the specimens A, B, and C with 15% tensile strain with the unstretched samples, the hardness of the core was 231 HV, 223 HV, and 219 HV in specimens A, B, and C, respectively. This means that, for the strain hardening during the same tensile deformation strain, the sample A (rod-shaped DCS-54%) is larger than sample B (plate-shaped DCS-54%), which is further larger than sample C (individual rod-shaped core) due to different constraining effects of the UFG shell.

The increment in hardness from the undeformed sample to the deformed sample in Fig. 11b and c were defined as ΔH (Fig. 11d), different ΔH values represent varying degrees of strain hardening during the stretching process. From Fig. 11d, one can see there exists a ΔH peak at the core/shell interface, indicating a strong interaction and strain

hardening at the interface. As the deformation increases, the hardness of the core gradually increases, and the ΔH peak at the interface region between hard shell and soft core decreases gradually, indicating a gradually weakened interaction at the interface. The average ΔH of the specimen C containing only the MG core at 15% strain is 24 HV, while the values of specimens A and B can reach 36 HV and 28 HV, respectively, indicating that the hardness of the soft core is affected (enhanced) by the hard UFG shell as a whole, especially in rod-shaped specimen A.

As for specimen B, by adding hard shells on two sides of the MG to design a simple sandwich structure material, although additional strengthening is provided due to the interaction between the two structures, its performance optimization is not as good as A, because its constraints are only reflected in the two-dimensional plane, indicates that the multi-directional stress state also plays an important role in the work hardening ability of the core.

In order to quantitatively explore the microstructural differences in uniform deformation of DCS2 with and without shell constraints, XRD and TEM examinations were performed on the core of specimens A and C at 15% strain (Fig. 12). During the deformation process of CG sample, deformation twinning will occur when dislocations accumulate to a certain extent. XRD patterns (Fig. 12a) were conducted on the cores of the specimens A and C to estimate the TB density (β) and dislocation density (ρ). β interpreted as the probability of twins appearing in two (111) planes, and can be calculated by Ref. [35]:

$$\beta = \frac{\Delta.C.G.(2\theta_{111}^\circ) - \Delta.C.G.(2\theta_{200}^\circ)}{11 \tan \theta_{111} + 14.6 \tan \theta_{200}} \quad (1)$$

$$\Delta.C.G.(2\theta_{hkl}^\circ) = (2\theta_{C.G.}^\circ - 2\theta_{max}^\circ)_{hkl} \quad (2)$$

where $2\theta_{C.G.}^\circ$ is the center of gravity of the peak, $2\theta_{max}^\circ$ is the angle corresponding to the maximum value of the diffraction peak.

The dislocation density ρ was evaluated by the modified Williamson-Hall method, based on the XRD data, as follows [36]:

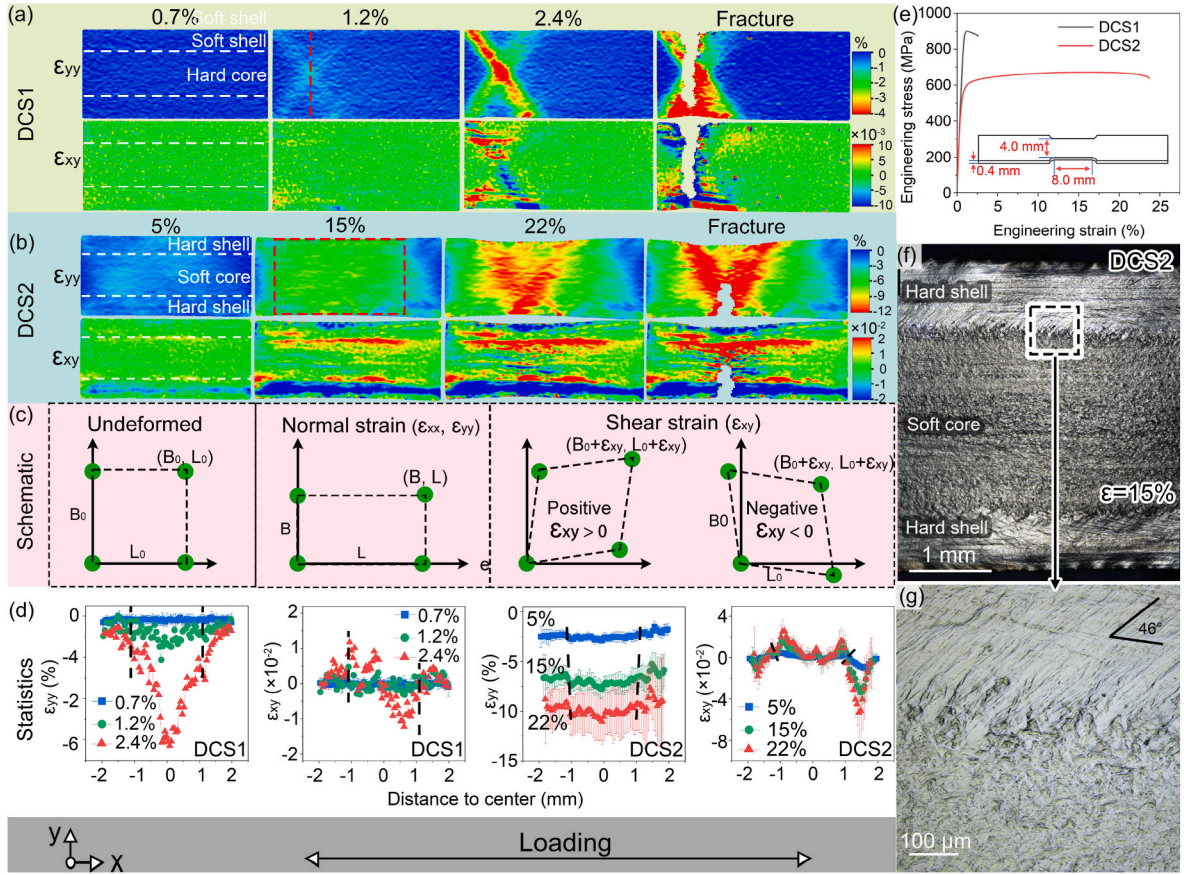


Fig. 9. DIC experimental results of DCS1 and DCS2 plate shaped specimen. (a,b) Distribution maps of normal strain (ϵ_{yy}) and shear strain (ϵ_{xy}) of DCS1 (a) and DCS2 (b) under different tensile deformation. The interface between the inner core and outer shell is marked by dotted white lines. (c) Schematic diagram of the surface lattice under the action of normal strain (ϵ_{xx} and ϵ_{yy}) and shear strain (ϵ_{xy}) during the tensile process. (d) Quantitative ϵ_{yy} and ϵ_{xy} distribution along the cross-section direction of the DCS1 and DCS2 plate shaped specimens, respectively. Specifically, for the DCS1 sample, quantitative results were taken from the red dashed section line in (a), and for the DCS2 sample, the quantitative results were averaged from 15 equal spacing section lines within the red dashed box in (b). The black dashed line represents the position of the soft/hard interface. (e) Tensile curves of plate specimens of DCS1 and DCS2 in DIC tests, the insert is the size of the tensile specimen. (f) Optical metallographic micrograph of DCS2 tensile specimen surface under tensile deformation of 15%. (g) Enlarged view of the area marked by black dotted line in (e). (For interpretation of the references to color in this figure legend, the reader is referred to the Web version of this article.)

$$\Delta K - \beta'W = \frac{0.9}{L} + \left(\frac{\pi A^2 b^2}{2}\right)^{\frac{1}{2}} \rho^{\frac{1}{2}} K \bar{C}^{\frac{1}{2}} + O(K^2 \bar{C}) \quad (3)$$

where $\Delta K = 2\cos\theta(\Delta d)/\lambda$, $K = 2\sin\theta/\lambda$, Δd is the width at half maximum (FWHM) (after subtracting the instrumental broadening), λ is the incident ray wavelength, corresponding to the cobalt target whose value of 0.1789 nm, β' is a parameter related to stacking fault (SFs) and TB density. W is the faulting-induced peak broadening at different hkl reflections, for (111), (200), (220), (311), and (222), the values of W were 0.433, 1, 0.707, 0.452, and 0.433, respectively. L is the average grain size, b is Burgers vector with a value of 0.256 nm in copper. A is a constant, in this work A is taken as 1 for all the specimens [37]. C is a contrast factor which depends on the elastic anisotropy of the material, it can be calculated by the following equation:

$$\bar{C} = \bar{C}_{h00}(1 - qH^2) \quad (4)$$

where $H^2 = (h^2k^2 + h^2l^2 + k^2l^2)/(h^2 + k^2 + l^2)^2$ for a cubic crystal system and q is a constant, when the material is copper and the ratio of edge dislocation to screw dislocation is equal, take $q = 2.01$ and $C_{h00} = 0.304$ [38]. The parameters L , ρ , and β' were then determined carefully to have the best linear fitting between ΔK and K , as shown in Fig. 12b. The estimated results show that A-core-15% > C-core-15% > C-core-0% in both values of ρ , and β' (Fig. 12c), this trend agree with the hardness values of the specimens A and C before and after stretching.

TEM and HRTEM further verify the above XRD results. As shown in Fig. 13, for the specimen A after 15% tensile deformation strain, high-density SFs and extremely fine nano-twins were observed within the grains. The annealing TBs in red region of Fig. 13b are no longer straight compared with those before stretching (Fig. 7i), and its HRTEM image shows that the TB exhibit a stepped shape, emitting SFs into the grains at kinks (Fig. 13b). The TBs of specimen C is relatively flat compared to A, HRTEM shows less SFs at the TBs, corresponding to fewer Shockley partial dislocation emissions (Fig. 13c and d).

4. Discussion

The above results indicate that the internal and external order of the soft and hard parts in the DCS Cu–Al alloy basically did not affect the strength which follows the rule-of-mixtures, however, seriously affect the ductility, and it seems that hard shell wrapped soft core can have higher ductility than the soft shell wrapped hard core. Moreover, the ductility is also closely related with the grain size/degree of softness and hardness/deformability of soft and hard parts. The combination of NG and UFG parts with low deformability seems not to be very good, although the NG shell wrapped UFG core still needs to be confirmed. The combination of NG/UFG and MG parts seems to be most beneficial to ductility, and it will be interesting to reveal the ductility of NG shell wrapped MG core.

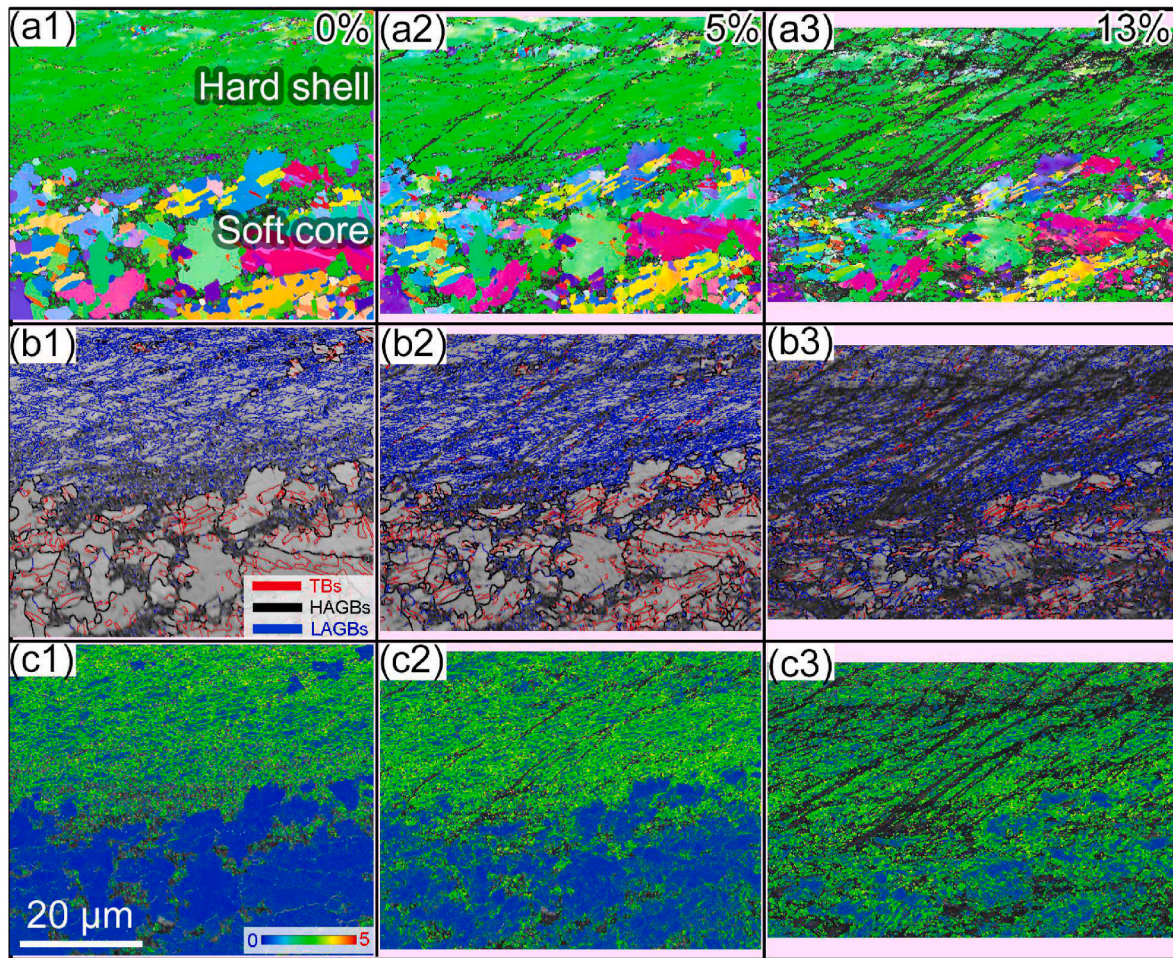


Fig. 10. EBSD maps of the core-shell interface in DCS2 tensile tested to different tensile strains. IPF (a1-a3), GB (b1-b3) and KAM (c1-c3) maps at 0% (a1, b1, c1), 5% (a2, b2, c2), and 13% (a3, b3, c3) tensile strains.

4.1. Construction of DCS materials

In this work, the DCS Cu–Al alloy with significant differences in microstructure and mechanical properties between the core and shell was prepared by plastic deformation through RS. In recent studies, RS is often used to carry out to achieve the purpose of strengthening the material [39–48]. In this study, the non-uniform distribution of strain in the radial direction during RS was mainly used to design and prepare the DCS Cu–Al alloy.

Through finite element simulation for RS in Fig. 14a [49], the stress distributions can be divided into three regions based on the stress situation of the circular section of the rod, i.e., Region I: compressive stress in both radial and axial directions. Region II: tensile stress in radial direction, most compressive stress with a small part of the tensile stress in axial direction, Region III: compressive stress in radial direction and tensile stress in axial direction. Moreover, the axial and radial compressive stresses in region I are similar, much higher than those in other regions, and it shows an approximate gradient distribution. In addition, sample DCS1 was obtained through multiple passes of RS deformation, and the gradual accumulation of strain resulted in a greater difference in the structure and properties between regions I and II, III.

Under this deformation, there are significant differences in the microstructure of FCC alloys with different SFE. Materials with higher SFE mainly exhibit dislocation slip during RS deformation, this results in a pyramid shaped gradient distribution of dislocation density and hardness in region I, while relatively uniform in regions II and III. such

as pure Cu [42]. However, due to the high grain refinement efficiency by twinning [50], the microstructure evolution of materials with low SFE is very sensitive to the processing conditions.

In the initial deformation stage of CG Cu–Al alloy, the critical shear stress required to trigger partial Shockley dislocations is greater than that of full dislocations, resulting in deformation dominated by dislocation slip. When the stress concentration caused by dislocation accumulation reaches a certain level, deformation twinning occurs, full dislocation multiplication is expected to be inhibited while partial dislocation is activated [51]. According to the pole mechanism [52], the critical shear stress τ_T required to activate a twin source can be calculated by:

$$n\tau_T = \frac{\gamma}{b_1} + \frac{Gb_1}{l} \quad (5)$$

where n is the stress concentration factor, and its value varies with the SFE. In Cu–Al alloy, a good match is achieved between experiments and estimates when $n = 1$ [53]. γ is the SFE of the alloy, while $b_1 = a/\sqrt{6}$ is the Burgers vector of Shockley partial dislocations, a is the lattice constant. G is the shear modulus, which is 44.5 GPa in Cu–Al alloy [54]. l is the length of the twin source. As the dislocation density increases, the dislocation length l will decrease, the relationship is $l = 1/\sqrt{\rho}$. Assuming that $l = l$, critical twinning stress can be written as:

$$n\tau_T = \frac{\gamma}{b_1} Gb_1\sqrt{\rho} \quad (6)$$

On the other hand, according to the Taylor dislocation hardening

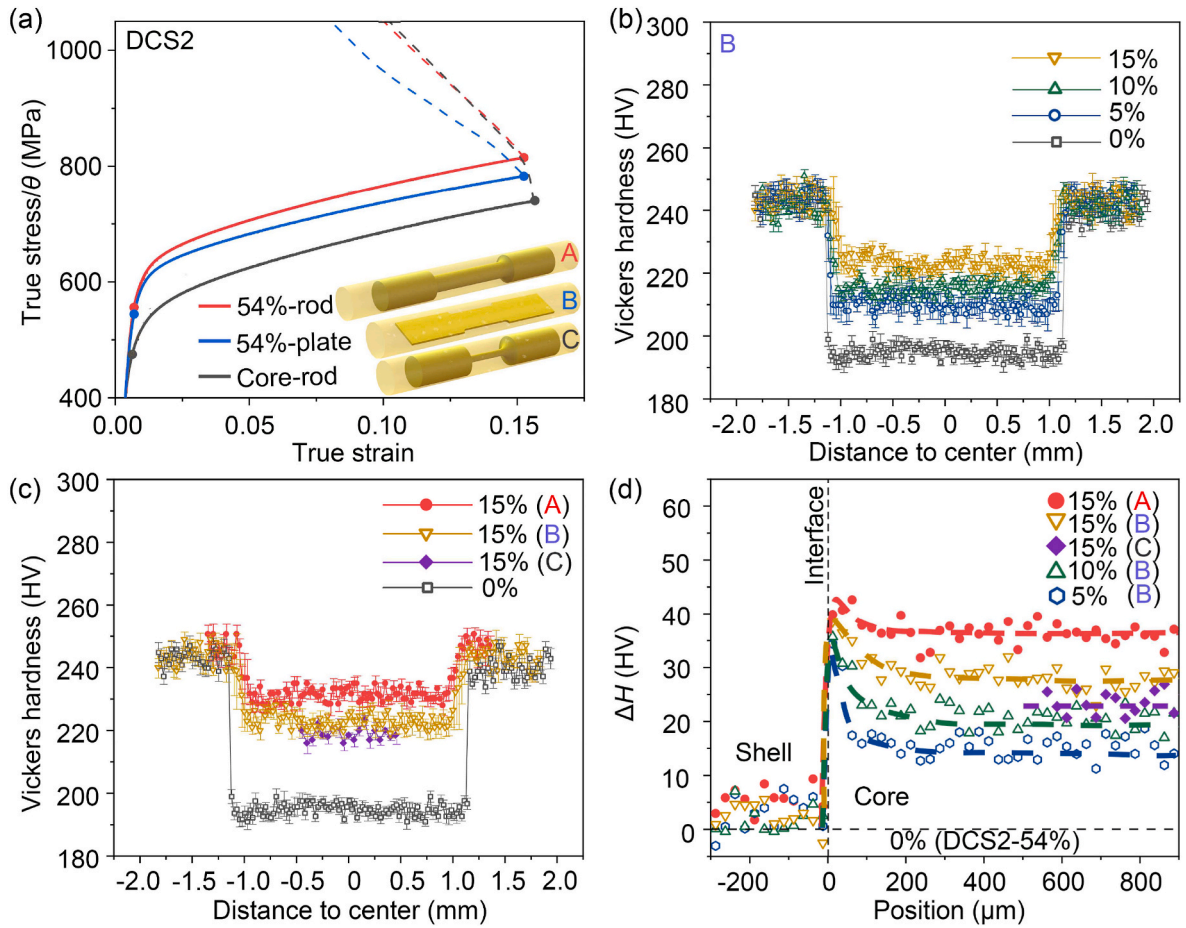


Fig. 11. Analysis of work hardening ability of sample DCS2. (a) The curves of true stress (solid line)/work hardening rate (dashed line) versus true strain of sample DCS2. The red, blue, and black lines correspond to 54%-rod (A), 54%-plate (B), and Core-rod (C) samples with red, blue, and black dots indicating the yield strength and UTS points of the three specimens, respectively. The insets show the sampling diagrams of the three samples. (b) Hardness distribution of specimen B under different tensile strains. (c) Hardness distribution of specimen A, B and C without tension and under 15% tensile strain. (d) ΔH versus position near the soft/hard interface after varying tensile strains. (For interpretation of the references to color in this figure legend, the reader is referred to the Web version of this article.)

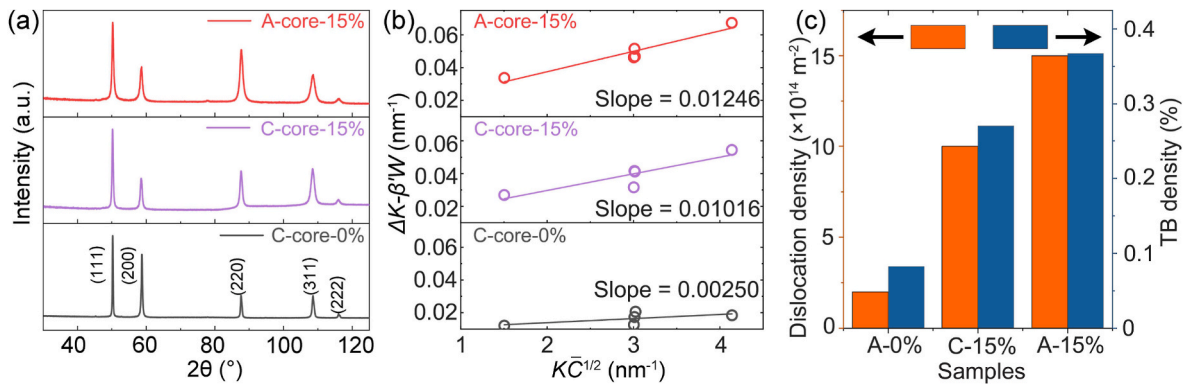


Fig. 12. XRD analysis of DCS2-54% materials. (a) XRD patterns of the MG cores with (A) and without shell (C) of DCS2-54% Cu-Al alloys in 0% and 15% tensile strain. (b) Fitting plot for dislocation density estimation based on XRD curves. (c) Dislocation and TB density estimated by XRD curves.

model [55], the relationship between local shear stress and dislocation density is:

$$\tau = \alpha G b \sqrt{\rho} \quad (7)$$

where $b = a/\sqrt{2}$ is Burgers vector of full dislocations. α is the empirical material constant, taken as 0.5 in this study [56]. Therefore, combining Eqs. (5)–(7), one can obtain the critical local dislocation density ρ_n

required for activating deformation twins [56]:

$$\rho_n = \frac{\gamma^2}{G^2 b_1^2 (nab - b_1)^2} \quad (8)$$

Based on Eq. (8), the ρ_n in this study by deforming CG Cu-Al alloy is $2.2 \times 10^{15} \text{ m}^{-2}$, which is close to the ρ_{GND} (about 90% total number of dislocations in severely deformed metals [57]) of DCS1-shell (Fig. 8), structurally manifested as twins and refined UFG in the SBs, while

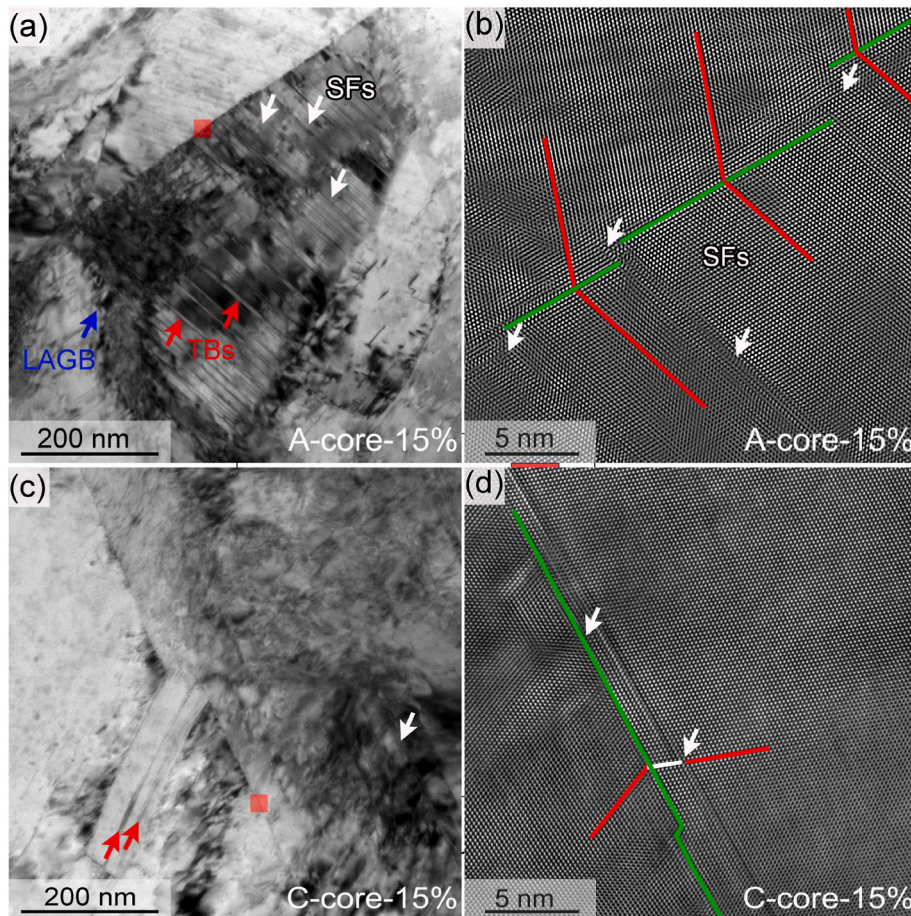


Fig. 13. Microstructural characterization of the deformed DCS-54% materials. (a) Typical TEM image of the MG core of specimen An under 15% tensile deformation strain. (b) Enlarged HRTEM image of red region in (a). (c) Typical TEM image of the individual MG core of specimen C under 15% tensile deformation strain. (d) Enlarged HRTEM image of red region in (c). (For interpretation of the references to color in this figure legend, the reader is referred to the Web version of this article.)

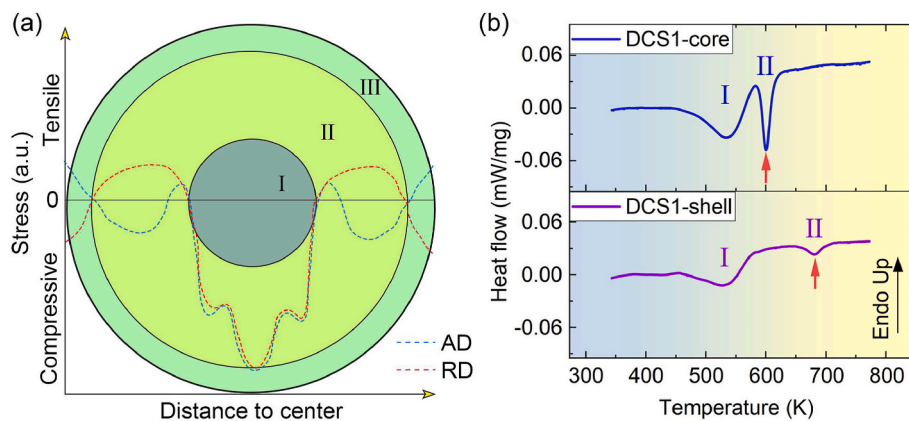


Fig. 14. (a) Finite element simulation of the distributions of axial and radial direction (AD and RD) stresses on the diameter of the top view of the RS rod [49]. (b) DSC curves of DCS1-core and DCS1-shell.

non-SBs region is mainly composed of dislocation cells, meaning that the stress state of shell cannot rely on twinning to refine grain size. The ρ_{GND} of the core far exceeds the value of ρ_n , indicating that under the high stress state of triaxial compression, refinement is mainly achieved through twinning. When most of the grains in region I are refined to NC grains by twinning due to high stress and strain accumulation, the gradient phenomenon is less obvious than that of RS pure copper [42], in other words, the gradient region is limited to the boundary between region I and region II. Therefore, Cu–Al alloys with a typical DCS1

structure were prepared.

The huge structural difference results in a difference in thermal stability between the DCS1-core and the DCS1-shell. Fig. 14b shows the DSC curves of the core and shell of DCS1. The two curves each have two clear exothermic peaks, according to the temperature dependence of dislocation density and grain size of NC alloys, the two exothermic peaks are connected to recovery and recrystallization, respectively [58]. The first exothermic peak (dislocation recovery) of both curves appears at 535 K, however, the second exothermic peaks (recrystallization) of the

core and shell appear at 600 K and 681 K, respectively. The strain energy of dislocations is related to the Burgers vector [59], and the recovery of dislocations does not require gestation period. This may be the reason why the recovery temperatures of the two samples with high dislocation density are the same. Unlike the recovery behavior, the temperature of recrystallization mainly depends on the stability of the GB structure. Due to the high GB excess energy in NC grains, the coarsening temperature of the NG grains in the core is lower than that of the shell containing a large amount of low-energy LAGBs. Moreover, the DSC exothermic enthalpies ΔH are different, for core, the ΔH of peak I and peak II are 10.4 J/g and 3.3 J/g, respectively, while for shell, the ΔH of peak I and peak II are 5.7 J/g and 1.0 J/g, respectively (see Table 3). Compared with the shell, the high ΔH value in the core represents higher dislocation density and GBs storage energy. Thus, we obtained the DCS2 sample by annealing. In addition, the in-situ generated DCS materials by this method have clean core-shell interface without any performance degradation caused by impurities at the interface in the composite material.

4.2. Deformation mechanisms of the DCS2-54%

4.2.1. The role of micro-shear bands of the shell

Micro-SBs play an important role in the deformation of this structural material, micro-SBs are usually formed in the severely deformed matrix which lacks strain hardening ability due to high dislocation density to alleviate strain concentration in the material and prevent material fracture [60]. However, when the dislocation density exceeds a certain level, a sudden increase in the number of local micro-SBs during plastic deformation of the material can easily cause necking of the materials, greatly reducing the uniform elongation of the materials. In literature, the MG was introduced into UFG matrix to alleviate this problem. The micro-SBs can be obstructed by the MG domain accompanied by high local strain, or can pass through or bypass the MG domain, resulting in a significant strain release [61]. Through the reasonable structure design, researchers can make good use of the micro-SBs as double-edged sword to improve the material performance. Such as uniform distribution of heterostructures induce the dispersion of micro-SBs to improve ductility [61], and gradient structure delays the rapid propagation of micro-SBs on the cross-section [60].

In this work, there are significant differences in grain size and dislocation density on both sides of the interface in our DCS2-54% Cu–Al alloy, and the MGs does not exist in the form of domains, but a macro cylinder with a diameter of millimeters. Compared with the core-shell interfaces of domains, the grains in the MG core have stronger coordinated deformation ability, which requires a great driving force for micro-SBs to pass through the interface. In other words, the micro-SBs in the UFG shell of DCS2-54% are completely pinned at the interface (Fig. 10), and the obvious shear strain at the interface of DCS2-54% indicates strong coordinated deformation between the core and shell, as shown in Fig. 9b. As the tensile strain increases, the range of the shear strain zone will gradually extend towards the core of the sample (Fig. 9d), which can alleviate the failure behavior caused by strain concentration and promoted strain delocalization [62], resulting in higher elongation than the rule-of-mixtures.

On the contrary, the DCS1 material has a lower strain hardening ability, even though there are obvious structural and performance differences between the core and shell. After yielding, the macro-SB rapidly led to necking in both core and shell (Fig. 9a), so DCS1 does not have the

Table 3

DSC exothermic peak temperatures (T) and exothermic enthalpies (ΔH) of the core and the shell of RS Cu–Al alloy with $\varepsilon = 2.5$.

Samples	Peak I		Peak II	
	T (K)	ΔH (J/g)	T (K)	ΔH (J/g)
Core	535	10.4	600	3.3
Shell	535	5.7	681	1.0

ability to block the SBs expansion at the interface, resulting in no evident increase in uniform elongation.

4.2.2. The complex stress state of the MG core

Fig. 15 provides a schematic comparison of the stress state and microstructure during the stretching process between DCS2-54% material with hard shell and soft core (right), and pure individual MGs material (left). The grains of pure MGs material are only subjected to uniaxial tensile stress during the stretching process, which is consistent with the stretching process of traditional homogeneous materials. While the MG core of DCS2-54% material was not only subjected to uniaxial tensile stress, but also constrained by the shell, which is reflected in the shear force inclined to the interface (purple arrows). This shear force can be further decomposed into compressive stress pointing perpendicularly to the axis (blue arrows). The complex stress state can activate more twinning and dislocation slipping and further increases their densities. Compared to the uniaxial stretching of the individual MG core, the hardness of the MG core in the sample DCS-54% after stretching increased by 12 HV (Fig. 11d).

4.2.3. Ductility increase by the extra strain hardening of the MG core

In the true stress-strain curve obtained at a constant strain rate, it is usually determined by the Considere criterion [63]:

$$\frac{d\sigma_t}{d\varepsilon_t} \geq \sigma_t \quad (9)$$

where σ_t , ε_t , and $(d\sigma_t)/(d\varepsilon_t)$ were the true stress, true strain, and work hardening rate θ , respectively. In the elastic deformation stage, with the rapid increase of σ_t , $(d\sigma_t)/(d\varepsilon_t)$ decreases rapidly. When plastic deformation is initiated, the changes of both are relatively gentle. As the tensile elongation increases, necking begins when the true stress-true

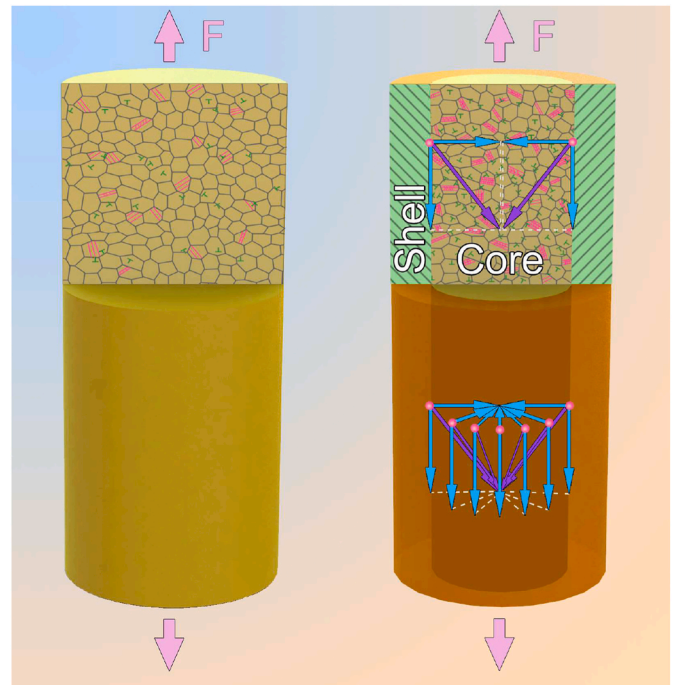


Fig. 15. Schematic diagram of force analysis on homogeneous MGs (left) and constrained MGs (right) by the hard UFG shell during stretching process. The pink lines, green ‘L’ symbols in the core, and black lines in the shell represent TBs, dislocations, and SBs, respectively. F represents the axial tensile stress, and the SBs of the shell produces an inclined stress on the MG core which further separates into a compressive and a shear stress at the interface. (For interpretation of the references to color in this figure legend, the reader is referred to the Web version of this article.)

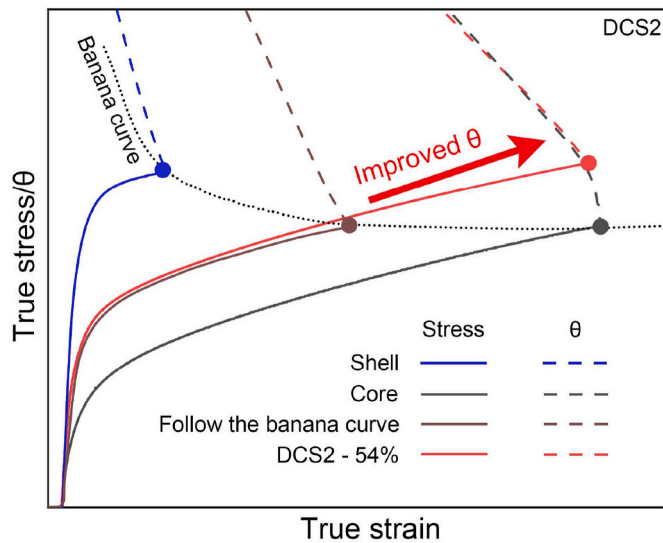


Fig. 16. Schematic diagram of true stress/strain hardening rate versus true strain based on the mechanical behavior of DCS2 material. The solid and dashed lines indicate true stress and strain hardening rate, respectively. The black dotted lines indicate the banana curve of uniform elongation followed by the rule-of-mixtures. The blue, black, and red lines indicate the individual shell, individual core, and DCS2-54% sample with the MG rod core wrapped by the hard shell from 360° without dead corners, respectively. (For interpretation of the references to color in this figure legend, the reader is referred to the Web version of this article.)

strain curve and work hardening rate-true strain curve contact at the same ϵ_b as shown in the schematic diagram of Fig. 16. For the MG samples with low dislocation density, due to their low yield strength and high work hardening ability, the two curves can intersect after a longer tensile deformation (black solid and dashed lines). For the UFG samples that have undergone severe plastic deformation, their high yield strength and low work hardening ability result in only a small amount of deformation strain with the two curves intersecting (blue solid and dotted lines).

The black dotted lines in the Fig. 16 indicate the banana curve of uniform elongation followed by the rule-of-mixtures. In this case, there is no interaction or coordinated deformation between the hard shell and soft core. Therefore, after mixing, the work hardening rate is lower than that of the individual MGs core due to the influence of the rule-of-mixtures, which causes the two curves of stress-strain and θ -strain to meet prematurely, and a much lower uniform elongation than that of the MG samples. To increase the uniform elongation of the DCS sample, additional strain hardening needs to be provided. As shown in Fig. 1, some materials with HCP structure can significantly increase the uniform elongation through activating $\langle c+a \rangle$ dislocations. For the FCC structured materials in this study, a significant increase in elongation to failure was successfully achieved by designing materials with dual-cable structure. The constraining effect from the shell to the core leads to higher dislocation and twin densities as well as work hardening ability in the core, thereby the overall ductility of the DCS-54% sample was improved.

5. Conclusions

In this work, based on the non-uniform distribution of deformation strain in the radial direction during rotary swaging and subsequent annealing, we designed two different types of macro DCS Cu–Al alloy rods. One has hard inner NG core (a grain size of 45 nm) and soft outer UFG shell (a sub-grain size of 300 nm), another has soft inner MG core (a grain size of 2.6 μm) and hard outer UFG shell. The inner NG/MG core has a diameter of 2.2 mm and the outer UFG shells have thicknesses of

0.4 and 0.9 mm, respectively. Systematic investigations were then performed including tensile tests, microstructural characterizations and deformation mechanism revealing. The main conclusions are as follows:

- (1) Both strength and ductility of the swaged DCS1-core, DCS1-30%, DCS1-54%, DCS1-shell follow linear rule-of mixtures.
- (2) The strength of the annealed DCS2-core, DCS2-30%, DCS2-54%, DCS2-shell follows linear rule-of mixtures, while ductility of DCS2-54% deviate evidently from linear rule-of mixtures, exhibiting excellent strength and elongation combinations and disrupting the strength-ductility trade-off relationship. By optimizing the stress state of the core during the stretching process, the original total ductility of 29.1% is increased to 31.9%.
- (3) Both NGs core and UFG shell in the DCS1 sample lack work hardening ability, which causes that their mixture does not have strong interaction under tensile deformation, therefore, their elongation to failure follows the rule-of-mixtures.
- (4) The MG core of the DCS2-54% sample blocks the propagation of the SBs of the UFG shell and maximizes its density. The UFG shell of DCS2-54% has a significant constraint effect on the MGs core, which greatly improved the ability to accumulate dislocations and nano-twins of the MG soft core, and improved the overall ductility.

CRediT authorship contribution statement

Kaixuan Zhou: Writing – review & editing, Writing – original draft, Methodology, Investigation. **Yonghao Zhao:** Writing – review & editing, Supervision, Investigation, Conceptualization. **Qingzhong Mao:** Writing – review & editing, Methodology. **Ruisheng Zhang:** Methodology. **Shunqiang Li:** Methodology. **Guosheng Sun:** Investigation. **Hongzhen Dong:** Methodology. **Lei Gu:** Methodology. **Jizi Liu:** Writing – review & editing, Investigation, Conceptualization.

Declaration of competing interest

The authors declare that they have no known competing financial interests or personal relationships that could have appeared to influence the work reported in this paper.

Data availability

Data will be made available on request.

Acknowledgements

The authors would like to acknowledge financial supports from National Key R&D Program of China (Grant No. 2021YFA1200203), National Natural Science Foundation of China (Grant No. 51971112, 51225102, and 52171119), Jiangsu Province Leading Edge Technology Basic Research Major Project (BK20222014), the Natural Science Foundation of Jiangsu Province (Grant No. BK20201308), and the Fundamental Research Funds for the Central Universities (No. 2023201001). The authors also want to acknowledge the support of the Jiangsu Key Laboratory of Advanced Micro-Nano Materials and Technology. SEM, TEM and EBSD experiments are performed at the Center of Analytical Facilities of Nanjing University of Science and Technology, XRD experiments are performed at eceshi (www.eceshi.com).

References

- [1] Liu C, Ye J, Wei X, Jin K-H, Wang J, Gao X, et al. Strength-ductility synergy in 3D-printed (TiB + TiC)/Ti6Al4V composites with unique dual-heterogeneous structure. *Compos Part B-Eng* 2023;266:111008.
- [2] Zhu YT, Liao X. Retaining ductility. *Nat Mater* 2004;3:351–2.
- [3] Gleiter H. Nanocrystalline materials. *Prog Mater Sci* 1989;33:223–315.

- [4] Tellkamp VL, Lavernia EJ, Melmed A. Mechanical behavior and microstructure of a thermally stable bulk nanostructured Al alloy. *Metall Mater Trans A* 2001;32:2335–43.
- [5] Legros M, Elliott BR, Rittner MN, Weertman JR, Hemker KJ. Microsample tensile testing of nanocrystalline metals. *Philos Mag A* 2000;80:1017–26.
- [6] Gu L, Meng A, Chen X, Zhao Y. Simultaneously enhancing strength and ductility of HCP titanium via multi-modal grain induced extra $c+a$ dislocation hardening. *Acta Mater* 2023;252:118949.
- [7] Chen W, Xiao B, Xu L, Han Y, Zhao L, Jing H. Additive manufacturing of martensitic stainless steel matrix composites with simultaneously enhanced strength-ductility and corrosion resistance. *Compos Part B-Eng* 2022;234:109745.
- [8] Li Z-B, Zhang H, Zhang G-H, Chou K-C. Superior strength-ductility synergy in a novel tailored Zr-based particle-strengthened medium W content alloys. *Compos Part B-Eng* 2022;236:109817.
- [9] Zhao YH, Bingert JF, Liao XZ, Cui BZ, Han K, Serhuceva AV, et al. Simultaneously elevating the ductility and strength of ultra-fine grained pure Cu. *Adv Mater* 2006;18:2949–53.
- [10] Lin D, Xi X, Ma R, Shi Z, Wei H, Song X, et al. Fabrication of a strong and ductile FeCoCrNiMo_{0.3} high-entropy alloy with a micro-nano precipitate framework via laser powder bed fusion. *Compos Part B-Eng* 2023;266:111006.
- [11] Fang TH, Li WL, Tao NR, Lu K. Revealing extraordinary intrinsic tensile plasticity in gradient nano-grained copper. *Science* 2011;331:1587–90.
- [12] Xiao Y, Yang Y, Wang D, Liu L, Liu Z, Wu S, et al. In-situ synthesis of high strength and toughness TiN/Ti6Al4V sandwich composites by laser powder bed fusion under a nitrogen-containing atmosphere. *Compos Part B-Eng* 2023;253:110534.
- [13] Wu XL, Yang MX, Yuan FP, Wu GL, Wei YJ, Huang XX, et al. Heterogeneous lamella structure unites ultrafine-grain strength with coarse-grain ductility. *Proc Natl Acad Sci USA* 2015;112(47):14501–5.
- [14] Ota M, Vajpai SK, Imao R, Kurokawa K, Ameyama K. Application of high pressure gas jet mill process to fabricate high performance harmonic structure designed pure titanium. *Mater Trans* 2015;56:154–9.
- [15] Lee TR, Chang CP, Kao PW. The tensile behavior and deformation microstructure of cryo-rolled and annealed pure nickel. *Mater Sci Eng* 2005;408(1–2):131–5.
- [16] Huang CX, Wang YF, Ma XL, Yin S, Höppl HW, Göken M, et al. Interface affected zone for optimal strength and ductility in heterogeneous laminate. *Mater Today* 2018;21(7):713–9.
- [17] Zhao Y, Topping T, Li Y, Lavernia EJ. Strength and ductility of bi-modal Cu. *Adv Eng Mater* 2011;13(9):865–71.
- [18] Wu XL, Jiang P, Chen L, Zhang JF, Yuan FP, Zhu YT. Synergetic strengthening by gradient structure. *Mater Res Lett* 2014;2(4):185–91.
- [19] Luo X, Feng ZQ, Yu TB, Luo JQ, Huang TL, Wu GL, et al. Transitions in mechanical behavior and in deformation mechanisms enhance the strength and ductility of Mg-3Gd. *Acta Mater* 2020;183:398–407.
- [20] Wei K, Hu R, Yin D, Xiao L, Pang S, Cao Y, et al. Grain size effect on tensile properties and slip systems of pure magnesium. *Acta Mater* 2021;206:116604.
- [21] Zhang Y, Tao NR, Lu K. Effects of stacking fault energy, strain rate and temperature on microstructure and strength of nanostructured Cu–Al alloys subjected to plastic deformation. *Acta Mater* 2011;59(15):6048–58.
- [22] Ran H, Jin RR, Wang YF, Wang MS, He Q, Guo FJ, et al. Optimizing the strength and ductility of Cu–Al alloy by an ideal grain structure. *Mater Sci Eng* 2021;807:140906.
- [23] An XH, Wu SD, Zhang ZF, Figueiredo RB, Gao N, Langdon TG. Enhanced strength–ductility synergy in nanostructured Cu and Cu–Al alloys processed by high-pressure torsion and subsequent annealing. *Scripta Mater* 2012;66(5):227–30.
- [24] Wang JJ, Tao NR. Comparison of tensile properties between nanotwinned and nanograned CuAl alloys. *Scripta Mater* 2018;149:16–20.
- [25] Wang JJ, Tao NR, Lu K. Revealing the deformation mechanisms of nanograins in gradient nanostructured Cu and CuAl alloys under tension. *Acta Mater* 2019;180:231–42.
- [26] Liu R, Tian YZ, Zhang ZJ, An XH, Zhang P, Zhang ZF. Exceptional high fatigue strength in Cu-15at.%Al alloy with moderate grain size. *Sci Rep* 2016;6:27433.
- [27] Tian YZ, Zhao LJ, Park N, Liu R, Zhang P, Zhang ZJ, et al. Revealing the deformation mechanisms of Cu–Al alloys with high strength and good ductility. *Acta Mater* 2016;110:61–72.
- [28] Tian YZ, Shibata A, Zhang ZF, Tsuji N. Ductility sensitivity to stacking fault energy and grain size in Cu–Al alloys. *Mater Res Lett* 2016;4(2):112–7.
- [29] Yin Z, Sun LL, Yang J, Gong YL, Zhu XK. Mechanical behavior and deformation kinetics of gradient structured Cu–Al alloys with varying stacking fault energy. *J Alloys Compd* 2016;687:152–60.
- [30] An XH, Wu SD, Wang ZG, Zhang ZF. Enhanced cyclic deformation responses of ultrafine-grained Cu and nanocrystalline Cu–Al alloys. *Acta Mater* 2014;74:200–14.
- [31] An XH, Lin QY, Wu SD, Zhang ZF. Improved fatigue strengths of nanocrystalline Cu and Cu–Al alloys. *Mater Res Lett* 2015;3(3):135–41.
- [32] Huang CX, Hu W, Yang G, Zhang ZF, Wu SD, Wang QY, et al. The effect of stacking fault energy on equilibrium grain size and tensile properties of nanostructured copper and copper–aluminum alloys processed by equal channel angular pressing. *Mater Sci Eng* 2012;556:638–47.
- [33] Kim JG, Baek SM, Cho WT, Song TJ, Chin K-G, Lee S, et al. On the rule-of-mixtures of the hardening parameters in TWIP-cored three-layer steel sheet. *Met Mater Int* 2017;23(3):459–64.
- [34] Zhao Y, Guo Y, Wei Q, Dangelewicz A, Xu C, Zhu Y, et al. Influence of specimen dimensions on the tensile behavior of ultrafine-grained Cu. *Scripta Mater* 2008;59(6):627–30.
- [35] Li XY, Zhou X, Lu K. Rapid heating induced ultrahigh stability of nanograned copper. *Sci Adv* 2020;6(17):eaaz8003.
- [36] Li YZ, Liang ZY, Huang MX. Strengthening contributions of dislocations and twins in warm-rolled TWIP steels. *Int J Plast* 2022;150:103198.
- [37] Wilhelm H, Paris A, Schafner E, Bernstorff S, Bonarski J, Ungar T, et al. Evidence of dislocations in melt-crystallised and plastically deformed polypropylene. *Mater Sci Eng* 2004;387–389:1018–22.
- [38] Ungár T, Dragomir I, Á Révész, Borbély A. The contrast factors of dislocations in cubic crystals: the dislocation model of strain anisotropy in practice. *J Appl Crystallogr* 1999;32(5):992–1002.
- [39] Wan YC, Tang B, Gao YH, Tang LL, Sha G, Zhang B, et al. Bulk nanocrystalline high-strength magnesium alloys prepared via rotary swaging. *Acta Mater* 2020;200:274–86.
- [40] Yang Y, Chen X, Nie JF, Wei K, Mao QZ, Lu FH, et al. Achieving ultra-strong Magnesium–lithium alloys by low-strain rotary swaging. *Mater Res Lett* 2021;9(6):255–62.
- [41] Chen X, Liu CM, Wan YC, Jiang SN, Chen ZY, Zhao YH. Grain refinement mechanisms in gradient nanostructured AZ31B Mg alloy prepared via rotary swaging. *Metall Mater Trans A* 2021;52(9):4053–65.
- [42] Mao QZ, Zhang YS, Guo YZ, Zhao YH. Enhanced electrical conductivity and mechanical properties in thermally stable fine-grained copper wire. *Commun Mater* 2021;2(1):1–9.
- [43] Mao QZ, Wang L, Nie JF, Zhao YH. Enhancing strength and electrical conductivity of Cu–Cr composite wire by two-stage rotary swaging and aging treatments. *Compos Part B-Eng* 2022;231:109567.
- [44] Mao QZ, Zhang YS, Liu JZ, Zhao YH. Breaking material property trade-offs via microdesign of microstructure. *Nano Lett* 2021;21(7):3191–7.
- [45] Lu FH, Nie JF, Ma X, Li YS, Jiang ZW, Zhang Y, et al. Simultaneously improving the tensile strength and ductility of the AlNp/Al composites by the particle's hierarchical structure with bimodal distribution and nano-network. *Mater Sci Eng* 2020;770:138519.
- [46] Yang Y, Nie JF, Mao QZ, Zhao YH. Improving the combination of electrical conductivity and tensile strength of Al 1070 by rotary swaging deformation. *Results Phys* 2019;13:102236.
- [47] Nie JF, Lu FH, Huang ZW, Ma X, Zhou H, Chen C, et al. Improving the high-temperature ductility of Al composites by tailoring the nanoparticle network. *Materialia* 2020;9:100523.
- [48] Meng A, Chen X, Nie JF, Gu L, Mao QZ, Zhao YH. Microstructure evolution and mechanical properties of commercial pure titanium subjected to rotary swaging. *J Alloys Compd* 2021;859:158222.
- [49] Kunčická L, Kocich R, Hervoches C, Macháčková A. Study of structure and residual stresses in cold rotary swaged tungsten heavy alloy. *Mater Sci Eng* 2017;704:25–31.
- [50] An XH, Lin QY, Wu SD, Zhang ZF. Microstructural evolution and shear fracture of Cu–16at.% Al alloy induced by equal channel angular pressing. *Mater Sci Eng* 2010;527(16–17):4510–4.
- [51] Xu W, Zhang B, Du K, Li XY, Lu K. Thermally stable nanostructured Al–Mg alloy with relaxed grain boundaries. *Acta Mater* 2022;226:117640.
- [52] Venables JA. Deformation twinning in face-centred cubic metals. *Philos Mag A* 1961;6(63):379–96.
- [53] Johari O, Thomas G. Substructures in explosively deformed Cu and Cu–Al alloys. *Acta Metall* 1964;12(10):1153–9.
- [54] Yang J, Ouyang P, Liu T, Yun H, Sun W, Wang Y, et al. First-principles study of the effect of aluminum content on the elastic properties of Cu–Al alloys. *Mater Today Commun* 2022;31:103399.
- [55] Taylor GI. The mechanism of plastic deformation of crystals. Part I.—theoretical. Containing papers of a mathematical and physical character. Series A: Proceedings of the Royal Society of London; 1934.
- [56] Huang CX, Wang K, Wu SD, Zhang ZF, Li GY, Li SX. Deformation twinning in polycrystalline copper at room temperature and low strain rate. *Acta Mater* 2006;54(3):655–65.
- [57] Liu Y, Cao Y, Mao Q, Zhou H, Zhao Y, Jiang W, et al. Critical microstructures and defects in heterostructured materials and their effects on mechanical properties. *Acta Mater* 2020;189:129–44.
- [58] Shen TD, Zhang J, Zhao Y. What is the theoretical density of a nanocrystalline material. *Acta Mater* 2008;56(14):3663–71.
- [59] Anderson PM, Hirth JP, Lothe J. Theory of dislocations. Cambridge University Press; 2017.
- [60] Yuan F, Yan D, Sun J, Zhou L, Zhu Y, Wu X. Ductility by shear band delocalization in the nano-layer of gradient structure. *Mater Res Lett* 2018;7(1):12–7.
- [61] Wang YF, Huang CX, He Q, Guo FJ, Wang MS, Song LY, et al. Heterostructure induced dispersive shear bands in heterostructured Cu. *Scripta Mater* 2019;170:76–80.
- [62] Wu H, Fan G. An overview of tailoring strain delocalization for strength-ductility synergy. *Prog Mater Sci* 2020;113:100675.
- [63] Zhu YT, Wu XL. Ductility and plasticity of nanostructured metals: differences and issues. *Mater Today Nano* 2018;2:15–20.